# Preliminary aeroelastic design of composite wings subjected to critical gust loads

Rajpal, D.; Gillebaart, E.; De Breuker, R.

**DOI**
10.1016/j.ast.2018.11.051

**Publication date**
2019

**Document Version**
Accepted author manuscript

**Published in**
Aerospace Science and Technology

# Preliminary Aeroelastic Design of Composite Wings Subjected to Critical Gust Loads

D.Rajpal[a,*], E. Gillebaart[a], R. De Breuker[a]

[a]*Department of Aerospace Structures and Computational Mechanics, Faculty of Aerospace Engineering, Delft University of Technology*

**Abstract**

Including a gust analysis in an optimization framework is computationally expensive as the critical load cases are not known a priori and hence a large number of points within the flight envelope have to be analyzed. Model order reduction techniques can provide significant improvement in computational efficiency of an aeroelastic analysis. In this paper, after thorough analysis of 4 commonly used model order reduction methods, balanced proper orthogonal decomposition is selected to reduce the aerodynamic system which is based on potential flow theory. The reduced aerodynamic system is coupled to a structural solver to obtain a reduced-order aeroelastic model. It is demonstrated that the dominant modes of the aerodynamic model can be assumed to be constant for varying equivalent airspeed and Mach number, enabling the use of a single reduced model for the entire flight envelope. A dynamic aeroelastic optimization method is then formulated using the reduced-order aeroelastic model. Results show that both dynamic and static loads play a role in optimization of the wing structure. Furthermore, the worst case gust loads change during the optimization process and it is important to identify the critical loads at every iteration in the optimization.

*Keywords:* Aeroelasticity, Structural Optimization, Gust Loads, Composite Wing

## 1. Introduction

The goals set out by the European Commission in the Flightpath 2050 report [1], include, among others, a 75% reduction in $CO_2$ emissions per passenger kilometer, 90% reduction in $NOx$ and 60% reduction in perceived noise by 2050 as compared to the aircraft in the year 2000. These objectives do not seem to be realistic for conventional designs as it is becoming increasingly difficult to make the well-known wing and tube configuration more efficient. Advanced technologies such as composite materials and aeroelastic tailoring along with novel designs seem to have the potential to address the required leap in performance. In the traditional design process, knowledge about the design increases, while the design freedom decreases as one goes from conceptual to preliminary and finally to the detailed design as shown in Figure 1. For conventional designs, the lack of knowledge during the initial stages is compensated through empirical knowledge. However, lack of such empirical knowledge for a novel design, results in the need for increased physics based knowledge during the initial design process.

In the case of a conventional aircraft wing, during the early stages, based on the empirical knowledge, static load cases due to manoeuvres are considered as the most critical loads that the aircraft will encounter. However, with the introduction of tailored composite materials, unsteady loads due to gusts can also become critical [2] and hence the need to include them in the initial design process. In this paper, the focus is to incorporate the effect of the dynamic gust loads in the preliminary structural design of the composite wings.

*Corresponding author.
Address: Kluyverweg 1, 2629 HS Delft, The Netherlands.
*Email address*: d.rajpal@tudelft.nl

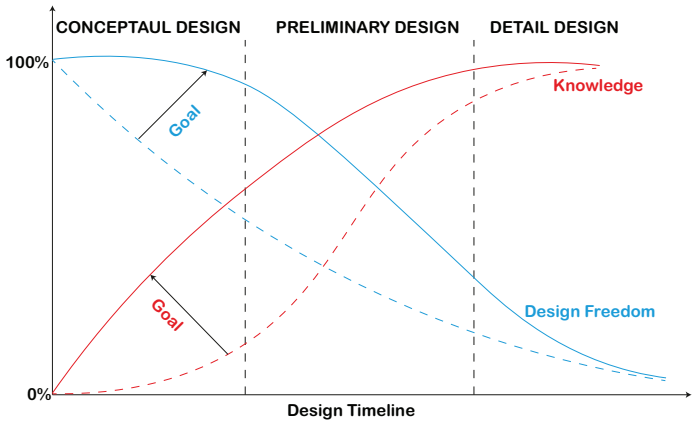


**Figure 1: Trend of knowledge and freedom in aircraft design process [3].**

Including the gust loads in an efficient and a reliable way during the initial phases of the design process is quite difficult. The first challenge is that there is no prior information on the flight points which will be critical with respect to dynamic loads. As per the requirements defined by the European Aviation Safety Agency (EASA) in the Certification Specifications for Large Aeroplanes (CS-25) [4], a range of load cases across the entire flight envelope has to be taken into consideration to determine the maximum loads the aircraft structure will experience. A ballpark approximation of the number of load cases to be taken into account can be in the order of 10 million [5]. This makes the process of finding the worst case gust loads computationally expensive. The second challenge is that as the design changes during optimization, the critical gusts might change as well and hence for every new iteration in the design process, the load cases have to be updated. This makes the inclusion of gust loads in the initial design process unfeasible.

The idea of improving the efficiency of the dynamic analysis has already received attention in recent years. Pototzky et al. [6] used the concept of matched filter theory from signal processing to identify worst case stochastic gust loads. Fidkowski [7] also applied matched filter theory in combination with the Lyapunov equation to identify critical load for the stochastic gust in the conceptual aircraft design process. Knoblach [8] used robust performance analysis from control theory to identify critical loads due to discrete 1-cosine gusts. In the work done under the European FP7 project FFAST [5, 9, 10], surrogate modelling, neural networks and optimization techniques were used for fast prediction of gust loads.

There has been a growing interest in using model order reduction (MOR) techniques to predict gust loads in an efficient way. The goal of the MOR techniques is to produce a system that shows similar aeroelastic response characteristics as the original, but consists of significantly fewer state variables, leading to a reduction in computational cost. Majority of the work done [11–15] was focused on using MOR techniques to reduce the computational fluid dynamics (CFD) models to predict the gust response. In the early stages of the design process, there is a need to evaluate a multitude of designs. Hence, even with MOR techniques, CFD can still be computationally expensive. The industry standard [16, 17], for dynamic loads, is the potential flow based aeroelastic solver such as MSC NASTRAN. There has not been sufficient focus in the literature on using the MOR methods for such solvers. Only recently Castellani et al. [18] applied MOR technique to the potential flow based aeroelastic system for rapid prediction of dynamic gust loads. For the determination of critical loads, Castellani et al. created a reduced aeroelastic model at different flight points and used interpolation techniques to cover the entire flight envelope.

In the present paper, the aeroelastic system is reduced by applying MOR method to the time-domain state-space unsteady vortex lattice model [19] and coupling it to the structural solver. To obtain a robust and accurate reduced-order model (ROM) for the aeroelastic analysis, four commonly used MOR methods for the reduction of the aeroelastic system, namely modal truncation (MT) [20, 21], balanced truncation (BT) [22], proper orthogonal decomposition (POD) [23], and balanced proper orthogonal decomposition (BPOD) [24, 25] are compared. These methods are used to produce a ROM of the aerodynamic model and their

performance is measured in terms of accuracy and robustness of the resulting model, and the computational cost of creating it and using it for simulation. The robustness of the methods is judged by determining the ability of the method to preserve the stability of the full-order model (FOM) and the amount of user input required to obtain a proper ROM. The method with the best performance is used to formulate the reduced-order aeroelastic model (ROAM), based on a global reduced aerodynamic basis, which is independent of equivalent airspeed and free stream Mach number. The advantage of such an approach is that the reduced basis needs to be calculated only once and thus the need for interpolation is avoided. This makes the determination of critical gust loads computationally efficient. The accuracy of the formulated ROAM is demonstrated by comparing the results with the responses from the FOM. Furthermore, an optimization framework is formulated using the ROAM which accounts for worst case gust loads at every iteration. To demonstrate the efficacy of such a framework, aeroelastic tailoring of the NASA Common Research Model (CRM) wing [26] is carried out. The innovations of this paper can be summarized as follows:

- Four commonly used MOR methods are compared, based on their application to a continuous time state-space unsteady vortex lattice model. The specific properties, accuracy, robustness and computational cost of the methods are investigated and compared.
- A ROAM is created, based on a global reduced aerodynamic basis independent of equivalent airspeed and free stream Mach number, for efficient aeroelastic loads analysis.
- An aeroelastic optimization method is formulated using the ROAM which has the capability to identify the critical loads at every iteration in the design process.

## 2. Aeroelastic Model

The ROAM is based on the framework of PROTEUS, in-house aeroelastic tool, developed at the Delft University of Technology. In PROTEUS, the wing is first divided into multiple spanwise sections, where each section is defined by laminates which can vary in the chord wise direction. A cross sectional modeller uses the laminate properties and the cross-sectional geometry to generate a Timoshenko cross-sectional stiffness matrices. A non linear aeroeasltic analysis is carried out for multiple load cases by coupling the geometrically nonlinear Timoshenko beam model to an unsteady vortex lattice aerodynamic model. A linear dynamic aeroelastic analysis is carried out around the nonlinear static equilibrium solution. In the post processing, the cross sectional modeller is used to retrieve the strains in the three-dimensional wing structure. Based on the applied strains in the structure, strength and buckling properties of the wing are calculated and fed to the optimizer as constraints. A detailed description of the PROTEUS is given in work by Werter and De Breuker [27]. In the following subsections, the formulation of ROAM has been described.

### *2.1. Aerodynamic model*

In PROTEUS, the aerodynamic model is continuous-time state-space unsteady vortex lattice method based on the work of Werter et al. [19]. The unsteady vortex lattice is an efficient method, of comparable fidelity to the doublet lattice method at moderate Mach numbers, but without some of its restrictions: the wake and planform can be non planar, flow tangency is imposed on the statically deformed geometry, and in-plane deformations are captured [28]. In the aerodynamic model, the wing is modelled as a thin wing with a prescribed wake using quadrilateral vortex rings with the collocation points in the center of the panels. Using the Kutta condition and Helmholtz theorem, a complete state-space system of equations for the potential flow is given by

$$\mathbf{A}\boldsymbol{\Gamma}^t = -\mathbf{V}_\infty \cdot \mathbf{n} \tag{1}$$

$$\boldsymbol{\Gamma}^t_{TE} = \boldsymbol{\Gamma}^t_{w_0} \tag{2}$$

$$\mathbf{H}_1\boldsymbol{\Gamma}^t = \mathbf{H}_2\boldsymbol{\Gamma}^{t-1} \tag{3}$$

where the matrix $\mathbf{A}$ contains the aerodynamic influence coefficients, $\mathbf{\Gamma}$ is the vector of unknown vortex ring strengths, $\mathbf{\Gamma}_{TE}$ is the vector of unknown vortex ring strengths at the trailing edge of the wing, $\mathbf{\Gamma}_{w_0}$ is the vector of unknown vortex ring strengths at the start of the wake, and matrices $\mathbf{H}_1$ and $\mathbf{H}_2$ describe the transport of vorticity in the wake.

The vector with vortex ring strengths $\mathbf{\Gamma}$ can be split into three separate sets of unknowns: the body, Kutta, and wake unknowns. Using this separation of unknowns, the system of equations can be rewritten into the form of the standard state equation of a state-space system:

$$\dot{\mathbf{x}}_a = \mathbf{A}_a \mathbf{x}_a + \mathbf{B}_a \mathbf{u} \tag{4}$$

where $\mathbf{A}_a$ is the aerodynamic state matrix, $\mathbf{B}_a$ is the aerodynamic input matrix, $\mathbf{u}$ is the input vector containing the time derivative of the angle of attack per aerodynamic panel of the wing, and $\mathbf{x}_a$ is the aerodynamic state vector containing the vortex strengths in the wake and angles of attack. The dot over the $\mathbf{x}$ indicates the time derivative. Combining Equation (4) with expressions for the unsteady lift and moment acting on the wing, state-space system can be formulated as

$$\begin{aligned} \dot{\mathbf{x}}_a &= \mathbf{A}_a \mathbf{x}_a + \mathbf{B}_a \mathbf{u} \\ \mathbf{y}_a &= \mathbf{C}_a \mathbf{x}_a + \mathbf{D}_a \mathbf{u} \end{aligned} \tag{5}$$

where $\mathbf{y}_a$ is the output vector containing the aerodynamic forces and moments acting on the wing per spanwise section. A more elaborate description of the aerodynamic modelling can be found in the work of Werter et al. [19].

### *2.2. MOR approach*

The dimension or order $n$, of a state-space system is given by the number of states in the vector $\mathbf{x}_a$. A system with more states generally requires a higher computational cost. Besides system size, sparsity and system structure are also of importance for the computational cost. In this study, the dimension of the system is typically in the order of $10^3 \sim 10^4$ and the matrices are densely populated due to the use of a boundary element method. The dimension of the matrices can be significantly reduced and sparsity increased by applying the MOR method. The general approach for a MOR of linear time-invariant (LTI) state-space systems is to project the original states onto a reduced basis:

$$\mathbf{x}_a = \mathbf{V}_r \mathbf{c} \tag{6}$$

where $\mathbf{c}$ is a vector with the $r$ reduced states and $\mathbf{V}_r$ is the $n \times r$ reduced basis onto which the original states are projected. Inserting Equation (6) into Equation (5) results in a system with $r \ll n$ states:

$$\begin{aligned} \dot{\mathbf{c}} &= \mathbf{V}_r^{-1} \mathbf{A}_a \mathbf{V}_r \mathbf{c} + \mathbf{V}_r^{-1} \mathbf{B}_a \mathbf{u} = \mathbf{A}_r \mathbf{c} + \mathbf{B}_r \mathbf{u} \\ \mathbf{y}_a &= \mathbf{C}_a \mathbf{V}_r \mathbf{c} + \mathbf{D}_a \mathbf{u} = \mathbf{C}_r \mathbf{c} + \mathbf{D}_a \mathbf{u} \end{aligned} \tag{7}$$

Since $\mathbf{V}_r$ is rectangular matrix of rank $r$, $\mathbf{V}_r^{-1}$ represents the pseudo inverse of $\mathbf{V}_r$. The number of states $r$ in the ROM depends on the required accuracy and the basis $\mathbf{V}_r$, but is typically in the order of $10 \sim 100$. Different MOR techniques can be used to find this reduced basis.

As mentioned in the introduction, four methods are compared here. The MT method originates from the field of structural dynamics. A selection of the eigenvalues of the system and their corresponding eigenvectors are used to create a reduced-order model. In structural dynamics, a clear physical interpretation for the eigenvectors is available. Even though this interpretation is less obvious in aerodynamics, the mathematical principle can still be applied [21, 29]. The resulting reduced system has the same eigenvalues as the states that are included, so the stability of the original system is always preserved. Furthermore, the only input required for the method to work is the order of the resulting ROM, making MT a very robust method.

The BT method is often used in control and simulation applications as a MOR tool. The states of a system can be described by the terms observability and controllability. The observability of a state describes

its influence on the output of the system in the absence of any input. Conversely, controllability describes how easily a state is excited by an input, when the system starts from rest. The principle of BT is to balance these two parameters, so that a state is equally observable as it is controllable [22]. The aerodynamic system that is used in this paper also has neutrally stable states, so the system has to be split into a stable and neutrally stable part. The neutral and stable part can be identified from the eigenvalue decomposition of the system, and they can be separated from each other. The BT method is applied to the stable system and after truncation the neutrally stable system is added again. The neutrally stable states are thus always included in the ROM. The truncation of the stable part of the system preserves its stability [30], so the combination of the neutrally stable part and the truncated part has the same stability characteristics as the original system. Similar to the MT method, this method requires no external input other than the required order of the ROM. These characteristics make the BT method very robust.

The principle of POD is rather simple. The response of the FOM to a certain input is simulated and at a number of points in time a snapshot is taken of the states of the system. This training data is used to find a basis for optimally approximating the data set. Even though this model provides an optimal approximation of the training data, its accuracy for inputs other than the training input depends on whether the required behavior is included in the simulation of the FOM. Furthermore, the method does not guarantee preservation of the stability characteristics of the original model. This makes the POD method less robust compared to the MT and BT methods.

In the BPOD method, certain analytical computations from the BT method are replaced by empirical approximations to speed up the process because BT is a relatively expensive method when larger systems have to be reduced. Combined with a projection method to reduce the number of outputs of the system [25], a significant improvement in computational cost can be obtained. Even though BPOD is an approximation of BT, it does not automatically mean that it will preserve the stability of the original model as BT does. However, it does typically suffer less from instabilities compared to POD [31]. The method is also dependent on empirical data, but this data is always the impulse response of the original system. This makes the method more robust than the POD method.

To compare the performance of the four methods, ROMs of the two aerodynamic systems are created, namely a heaving wing and an accelerating wing.

*2.2.1. Heaving wing*

The first test case is a rectangular heaving wing with an aspect ratio of 4. The wing oscillates up and down with a specific reduced frequency, creating a periodic aerodynamic response. The wing is discretized into 40 elements in chordwise direction and 10 in the spanwise direction. The wake, with a length of 10 times the chord, is automatically discretized into 203 elements in the chordwise direction, resulting in 2,030 state variables. The reduced frequency of the oscillation is computed as follows:

$$k = \frac{\omega b}{V_\infty} \tag{8}$$

where $\omega$ is the frequency of the oscillation in rad/s, $b$ is the airfoil half chord, and $V_\infty$ is the freestream velocity. The heaving amplitude is equal to 10% of the chord.

The variations in lift and moment coefficients in time are computed with the FOM and the four ROMs. Figures 2 and 3 show the comparison for a reduced frequency of 0.1. All the ROMs are formed using 100 mode shapes. Data from the FOM for a similar oscillating wing is used as training data for the POD ROM.

The lift coefficient curves of the ROMs all lie very close to the FOM. The curve of the MT method has the largest deviation, as is demonstrated in the next paragraph. For the moment coefficient curve of the MT method, the deviation from the FOM is more pronounced. In contrast to the lift coefficient, the moment coefficient is strongly influenced by the pressure distribution on the wing. On inspection of the mode shapes resulting from the method, an explanation for this effect can be found. The mode shapes stay close to zero at the start of the wake and grow towards the end of the wake. At higher mode shapes this effect becomes more clear, as can be seen in Figure 4. Accurately approximating the variation of the state

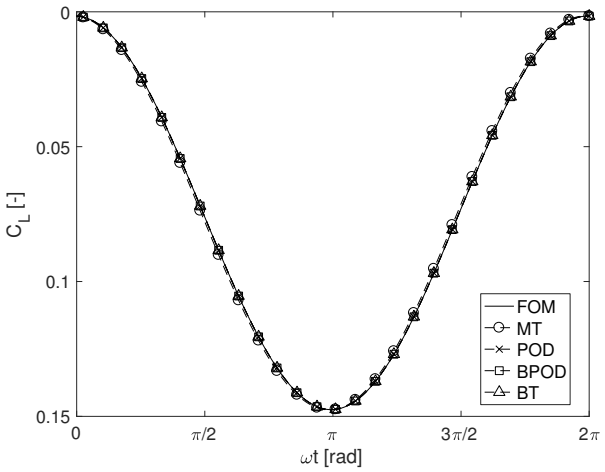


**Figure 2: Lift coefficient variations in time for a flat wing with $\mathcal{AR}$= 4 and k = 0.1.**

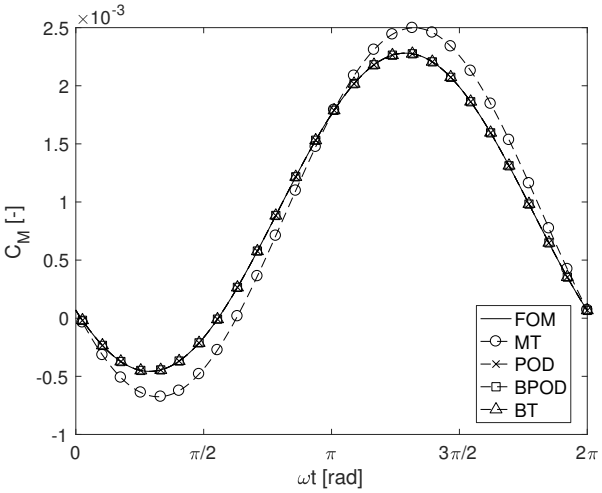


**Figure 3: Moment coefficient variations in time for a flat wing with $\mathcal{AR}$= 4 and k = 0.1.**

variables in the wake is impossible with these modes since variations at the beginning of the wake cause large oscillations at the rear. This problem is illustrated in Figure 5. The first part of the wake response is accurately reproduced by the ROM, but towards the end of the wake the ROM response starts to oscillate around the FOM response.

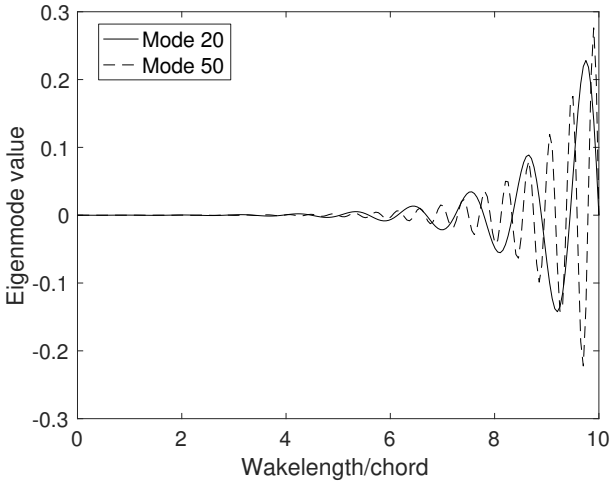


**Figure 4: Higher MT mode shape distributions over the wake of a 2-dimensional airfoil.**

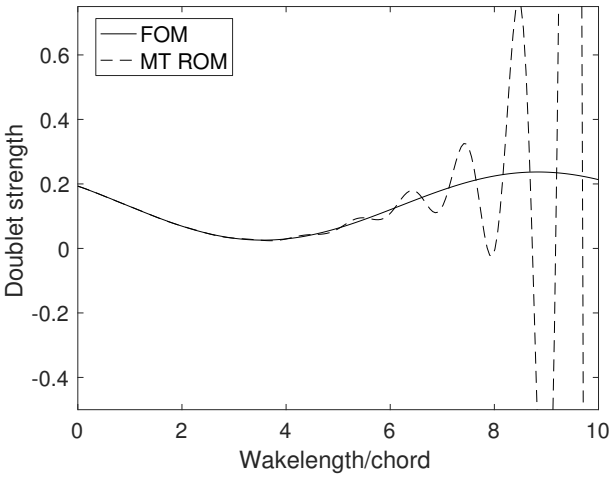


**Figure 5: Comparison of the wake response of the FOM and the MT ROM for a point in time.**

Behbahani-Nejad and Changizian [32] have also encountered oscillations in the wake when they applied MT to a model of an unsteady partial cavity flow. Calculating the cavity length and lift coefficient for these flows required an accurate approximation of the wake response. The results showed that these parameters could only be accurately approximated when all mode shapes were included in the ROM, resulting in a model which is exactly the same as the FOM. The problem is not mentioned in other literature on the application of MT to unsteady aerodynamics, most likely because an accurate reproduction of the wake response turns out to be less important for lift calculations of an airfoil or wing, as will be shown for the test cases. Because of this mode shape behaviour, the MT method is unable to reproduce the wake response accurately resulting in an inaccurate pressure distribution and thus, combined with the deviation in the lift, a large deviation in the moment coefficient is observed.

The convergence of the ROM with increasing number of included mode shapes is evaluated using the root-mean-square error (RMSE) between the FOM and ROM results, resulting in Figure 6. The MT method

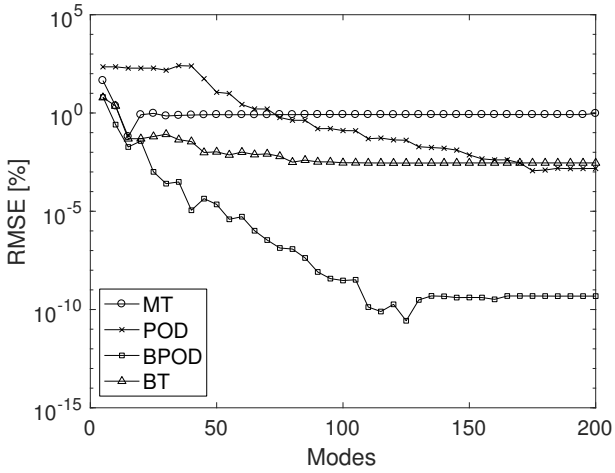


**Figure 6: Lift coefficient RMSE for the heaving wing test case with k = 0.1.**

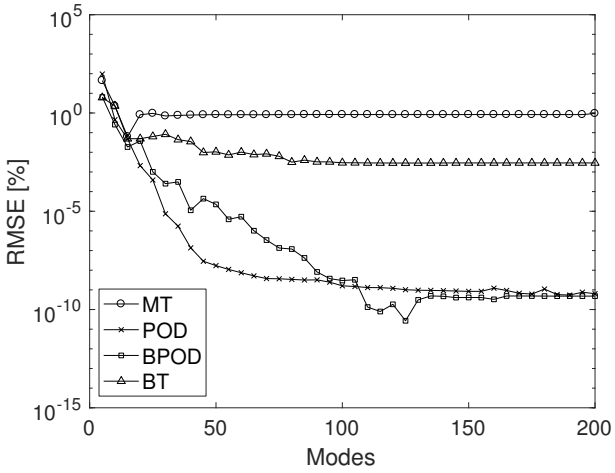


**Figure 7: Lift coefficient RMSE for the heaving wing test case with k = 0.1, using exact FOM data as training data for POD.**

converges fast up to 15 modes, but diverges when more modes are included. This divergence is caused by the phenomenon that was already shown in Figure 5. The oscillating wake causes inaccuracies in the solution. Only when a large portion of all modes are included in the ROM does it slowly start to converge again, because the oscillations start to cancel each other out. When the final few modes are included it converges more rapidly again. This last behavior is not shown in Figure 6.

The convergence of the BPOD method is superior for this test case. Whereas the error of the other methods levels off relatively soon, it keeps decreasing to a RMSE of $10^{-10}$ % for BPOD. The method also outperforms BT on this aspect, even though it is an approximation of the latter. An explanation for this result is that larger systems become more ill-conditioned, due to the larger differences in aerodynamic influence coefficients. Both the MT and BT methods inverse the right eigenvector matrix to obtain the left eigenvector matrix. This step becomes inaccurate for larger systems, due to the ill-conditioning of the eigenvector matrix. The BPOD method does not require this step and thus remains more accurate. This problem is clearly visible in the modal residuals computed with Equation (9)

$$R = ||\mathbf{V}^{-1}\mathbf{A}\mathbf{V} - \mathbf{\Lambda}|| \tag{9}$$

where $\mathbf{V}$ is a matrix with the right eigenvectors as columns and $\mathbf{\Lambda}$ is a matrix with the eigenvalues on its diagonal. Both the MT and BT method produce the same modal residuals, which are shown in Table 1 for variations in spanwise and chordwise elements. The residual significantly increases for a larger system, resulting in the reduced accuracy of the two methods.

**Table 1: Modal residuals of MT and BT for varying numbers of chordwise (nbc) and spanwise (nbs) elements.**

| | **nbc = 10** | **nbc = 20** | **nbc = 40** |
|---|---|---|---|
| **nbs = 2** | $8.3 \cdot 10^{-8}$ | $2.5 \cdot 10^{-2}$ | $1.5 \cdot 10^{1}$ |
| **nbs = 4** | $5.2 \cdot 10^{-7}$ | $1.4 \cdot 10^{-1}$ | $3.4 \cdot 10^{1}$ |
| **nbs = 8** | $4.8 \cdot 10^{-6}$ | $7.3 \cdot 10^{1}$ | $7.3 \cdot 10^{1}$ |

The accuracy of the POD method is low for a small number of included modes. The result gradually converges to that of the FOM as more modes are included. However, it is observed that the training data can have a large influence on the convergence behavior of this method. In the previous section, it was

mentioned that the POD method obtains a reduced basis that approximates the original data set in an optimal way. Consequently, if the exact data of the FOM for this test case is used, the POD method performed approximately on par with the BPOD method, as Figure 7 shows. These results demonstrate the importance of selecting the right training data, as the accuracy of simulations outside the scope of the training data will suffer from reduced accuracy. Working in the frequency domain would reduce the challenge of selecting the best training data as the selection is based on frequencies instead of time-domain disturbances [33, 34]. Choosing the range of frequencies of interest will provide a ROM which is accurate in this range.

Figure 8 shows the convergence of the moment coefficient and looks similar to Figure 6. The main difference is the larger effect of the inaccuracy of the MT and BT methods, due to the system size. Their convergence flattens out at a higher RMSE compared to the lift coefficient convergence.

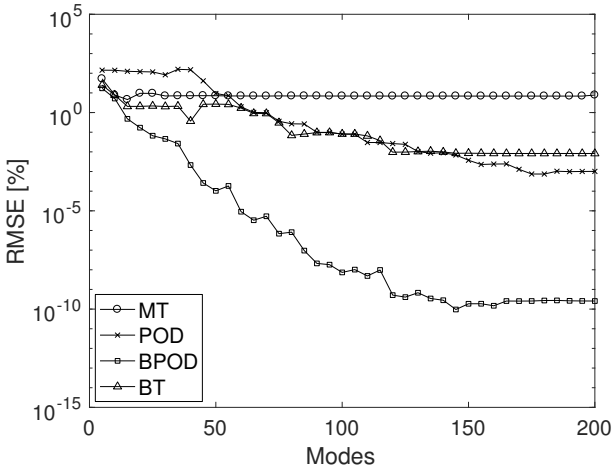


**Figure 8: Moment coefficient RMSE for the heaving wing test case with k = 0.1.**

To make a fair comparison of the computational cost involved with the MOR methods, they are set up to have a maximum RMSE of 0.1% for both the lift and moment coefficient. Figure 8 shows that for MT this accuracy cannot be achieved, so the optimum at 15 modes is used. The computations are performed on a PC with an Intel Core i5-3470 processor and 4 GB of memory using MATLAB R2013b. The cost of computing the ROM and of simulating it, listed in Table 2, show that these MOR methods can significantly reduce the cost of the aerodynamic analysis when multiple analyses have to be performed with the same model. In, for example, a gust load analysis of a wing, hundreds or even thousands of different conditions have to be analyzed and these ROMs can provide a large saving in computational cost. The last column of Table 2 shows after how many simulations a profit in computational time is gained compared to the FOM, taking into account both the extra cost related to the formulation of the ROM and reduced cost of the simulation. Please note that even though the MT method has the lowest break even number, its accuracy is approximately one order of magnitude lower compared to the other methods.

**Table 2: Computational cost of building the ROMs and simulating it compared to the cost of simulating the FOM.**

| Method (states) | Building ROM [s] | Simulation [s] | Break even number |
|---|---|---|---|
| FOM (2030) | - | 6.2 | - |
| MT (15) | 22.4 | 0.005 | 4 |
| POD (89) | 66.1 | 0.012 | 11 |
| BPOD (22) | 61.8 | 0.005 | 10 |
| BT (78) | 631.3 | 0.012 | 102 |

The computational cost for building the ROM strongly depends on the size of the original system. The

three parameters determining the size of the system are the number of body elements in the spanwise and chordwise direction, and the length of the wake. Figures 9a to 9c show the variation of the computational cost for variations in these parameters. All the methods show a close to a cubic relation between the

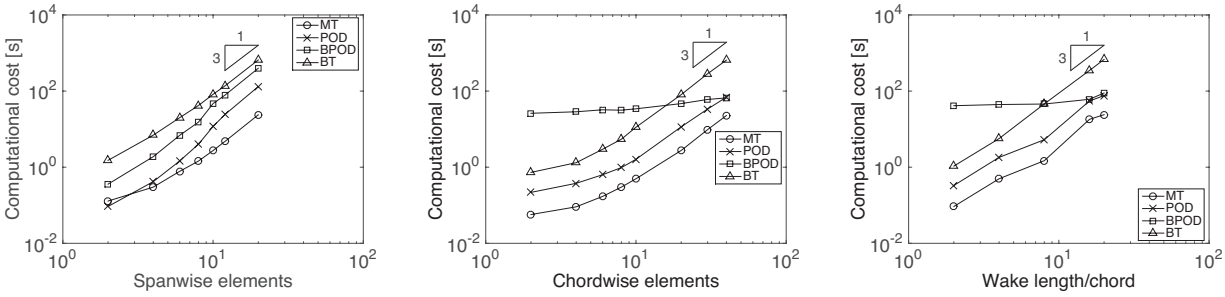


**(a) Spanwise elements** **(b) Chordwise element** **(c) Wake length**

**Figure 9: Computational cost as a function of discretization for the heaving wing test case.**

computational time and the number of spanwise elements. However, for the other two parameters the BPOD method deviates from this trend. It seems to be insensitive to the number of chordwise element and the length of the wake. This can be explained by the way the BPOD ROM is computed. The computational time required for this method is dominated by the singular value decomposition (SVD) of the product of the direct and adjoint impulse data matrices. Even though the size of these matrices themselves depends on all of the parameters, the product only depends on the number of spanwise elements. The influence of the other two parameters is thus only seen in the impulse simulation time, which is only a small portion of the full computational cost.

*2.2.2. Accelerating wing*

The second benchmark is a rectangular wing experiencing an instantaneous acceleration from zero to a constant velocity. The wing, with an aspect ratio of 6, is discretized into 50 elements in chordwise and 10 elements in the spanwise direction. The wake is discretized into 127 elements in the chordwise direction and has a length of 5 times the chord, generating a system with 1,270 states.

The BT and BPOD methods recreate the FOM response very accurately, whereas the MT and POD methods have some difficulties, as can be seen in Figure 10a. All four responses are obtained using 50 modes. At the start, the MT ROM deviates significantly from the FOM, but as time progresses it converges and matches the FOM response almost exactly. From Figure 10a it seems that the POD ROM slowly converges to the FOM solution, but when a longer time period is plotted it becomes clear that it does not. On inspection of the eigenvalues of the reduced system this is confirmed, as multiple of them have a positive real part and are thus unstable. This instability can be solved by increasing the number of mode shapes included in the ROM. The POD response shown in Figure 10b, obtained using 100 modes, is still not very close, but no longer diverges. It can also be seen that the MT ROM converges slightly faster to the FOM compared to when 50 modes are included.

From the test cases presented here, the conclusion can be drawn that BPOD is the most suitable method for reducing the aerodynamic model. The method combines high accuracy at low numbers of states with a relatively low computational cost and good robustness. The other methods all show problems in at least one of these characteristics. For the remainder of the paper, the BPOD method is thus used for the reduction of the aerodynamic model within the aeroelastic framework.

*2.3. Reduced Order Aerodynamics*

For the determination of critical loads, the aeroelastic system must be solved over a large number of flight points to calculate the various responses of the aircraft over the entire flight envelope. A significant saving in computational expense can be achieved if a reduced-order aeroelastic system can be used instead

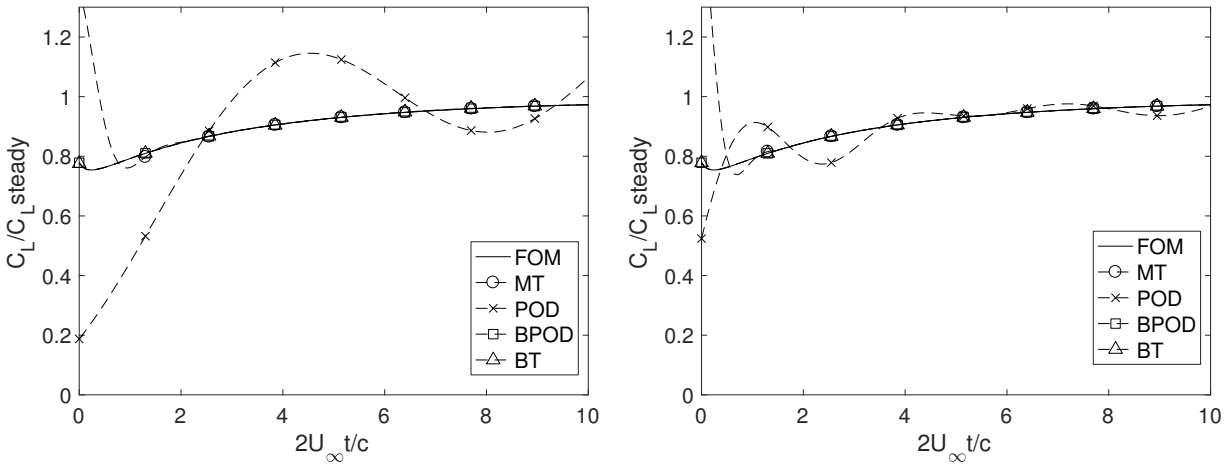


**(a) 50 modes** **(b) 100 modes**

**Figure 10: Lift response for a suddenly accelerated, flat wing with $\mathcal{AR}$= 6.**

of a full order system. However, the full order aerodynamic system depends on parameters such as altitude, Mach number and velocity, hence every new flight point would necessitate a new ROAM. Thus an efficient way of applying the reduced-order aeroelastic system without the need of performing a new reduction at each flight point has been formulated.

Benner et al. [35] have provided a comprehensive survey on MOR for a parametric state-space system. Generally, the approaches for the parametric model order reduction can be differentiated into local and global based methods. In the local based methods [36, 37], the reduced basis required at a given point can be generated by interpolating local reduced bases generated at a fixed number of points in the parameter space. In the global based methods [38], a single reduced basis is generated by projecting the global matrix containing snapshots at various points in the parameter space. By projecting a global matrix, dominant modes across entire parameter space are selected, thus giving a good approximation. For the current aerodynamic system, a method similar to the global based methods is used. A reasonable assumption can be made that, for a given wing planform, the dominant aerodynamic modes will be the same for all the points inside the flight envelope. The basis for this assumption is explained below.

For every point inside the flight envelope, the aerodynamic state-space matrices depend upon the equivalent air speed ($V_{eq}$), and the free stream Mach number, $M$. For the assumption to be valid, the dominant modes of the aerodynamic system should not change with a change in $V_{eq}$ and $M$. With respect to $V_{eq}$, the aerodynamic system of equations described in Equations 1, 2 and 3 can be reformulated as

$$\mathbf{K}_1\mathbf{\Gamma}_b + \mathbf{K}_2\mathbf{\Gamma}_{w_0} + \mathbf{K}_3\mathbf{\Gamma}_w = -\mathbf{V}_\infty\mathbf{n}_x - \mathbf{V}_\infty\mathbf{n}_z\boldsymbol{\alpha} \tag{10}$$

$$\mathbf{K}_4\mathbf{\Gamma}_b + \mathbf{K}_5\mathbf{\Gamma}_{w_0} = 0 \tag{11}$$

$$\mathbf{K}_6(V_{eq})\mathbf{\Gamma}_w + \mathbf{K}_7(V_{eq})\mathbf{\Gamma}_{w_0} = \dot{\mathbf{\Gamma}}_w \tag{12}$$

where $\mathbf{K}_1$, $\mathbf{K}_2$ and $\mathbf{K}_3$ are a parts of the aerodynamic influence coefficient (AIC) matrix, $\mathbf{K}_4$ and $\mathbf{K}_5$ connect the trailing edge panel to the first wake panel satisfying the Kutta condition, and $\mathbf{K}_6$ and $\mathbf{K}_7$ describe the transport of vorticity in the wake. The subscripts $b$ and $w$ indicate the body and wake, respectively. Both $\mathbf{K}_6$ and $\mathbf{K}_7$ depend on $V_{eq}$. The AIC matrix also depends upon the velocity. A change in velocity necessitates a change in the trim angle, which leads to a change in angle between the body and the wake and thus a change of the AIC matrix. However, in a linear analysis, for small deviations in the trim angle, the AIC matrix can be assumed to be constant. Expressing $\mathbf{\Gamma}_b$ and $\mathbf{\Gamma}_{w_0}$ as function of $\mathbf{\Gamma}_w$, the state equation of state-space system can be derived as

$$\dot{\mathbf{\Gamma}}_w = \mathbf{K}_8(V_{eq})\mathbf{\Gamma}_w + \mathbf{K}_9(V_{eq})\boldsymbol{\alpha} + \mathbf{K}_{10}(V_{eq}) \tag{13}$$

where $\mathbf{K}_8$, $\mathbf{K}_9$ and $\mathbf{K}_{10}$ have linear dependencies on equivalent airspeed.

To compute the aerodynamic output, forces and moments are split into steady component and an unsteady component. The steady component of the aerodynamic forces is given by

$$\mathbf{F}_{st} = \rho \mathbf{V}_\infty \times \mathbf{\Gamma} = \rho \mathbf{V}_\infty \times \mathbf{e}_\Gamma \Gamma \tag{14}$$

where $\mathbf{e}_\Gamma$ is the vector along the vortex segment and $\Gamma$ is the vortex strength of the vortex segment. The unsteady component of the aerodynamic forces is given by

$$\mathbf{F}_{unst} = \rho \widehat{\mathbf{V}}_\infty \times \widehat{\mathbf{e}}_\Gamma \frac{\partial \Gamma_{i,j}}{\partial t} \mathbf{H}_{i,j} \tag{15}$$

where $\widehat{\mathbf{V}}_\infty$ is the unit vector in the direction of the free stream velocity, $\widehat{\mathbf{e}}_\Gamma$ is the unit vector in the direction of the leading vortex segment and $\mathbf{H}$ is the AIC matrix. By defining a reference axis with respect to which the aerodynamic moments are computed, the total aerodynamic forces and moments are expressed as

$$\begin{bmatrix} \mathbf{F}_a \\ \mathbf{M}_a \end{bmatrix} = \begin{bmatrix} \mathbf{F}_{st} \\ \mathbf{M}_{st} \end{bmatrix} + \begin{bmatrix} \mathbf{F}_{unst} \\ \mathbf{M}_{unst} \end{bmatrix} = \mathbf{L}_1(V_{eq})\mathbf{\Gamma}_b + \mathbf{L}_2(V_{eq})\dot{\mathbf{\Gamma}}_b \tag{16}$$

where $\mathbf{L}_1$ and $\mathbf{L}_2$ have linear dependencies on equivalent airspeed. Relating $\mathbf{\Gamma}_b$ to $\mathbf{\Gamma}_w$ leads to

$$\begin{bmatrix} \mathbf{F}_a \\ \mathbf{M}_a \end{bmatrix} = \mathbf{L}_9(V_{eq})\mathbf{\Gamma}_w + \mathbf{L}_{10}(V_{eq})\alpha + \mathbf{L}_8(V_{eq})\dot{\alpha} + \mathbf{L}_{11}(V_{eq}) \tag{17}$$

Using Equations 13 and 17, the aerodynamic state-space equation is given as

$$\begin{aligned} \dot{\mathbf{x}}_a &= \begin{bmatrix} \mathbf{K}_8(V_{eq}) & \mathbf{K}_9(V_{eq}) \\ 0 & 0 \end{bmatrix} \mathbf{x}_a + \begin{bmatrix} 0 & \mathbf{K}_{10}(V_{eq}) \\ \mathbf{I} & 0 \end{bmatrix} \mathbf{u}, \\ \mathbf{y}_a &= \begin{bmatrix} \mathbf{L}_9(V_{eq}) & \mathbf{L}_{10}(V_{eq}) \end{bmatrix} \mathbf{x}_a + \begin{bmatrix} \mathbf{L}_8(V_{eq}) & \mathbf{L}_{11}(V_{eq}) \end{bmatrix} \mathbf{u}, \end{aligned} \tag{18}$$

Thus the aerodynamic system can be assumed to have an affine dependency on the velocity. The aerodynamic state-space system can then be formulated as

$$\begin{aligned} \dot{\mathbf{x}}_a &= \mathbf{F}_1(V_{eq})\hat{\mathbf{A}}_\mathbf{a}\mathbf{x}_a + \mathbf{F}_2(V_{eq})\hat{\mathbf{B}}_a\mathbf{u}, \\ \mathbf{y}_a &= \mathbf{F}_3(V_{eq})\hat{\mathbf{C}}_a\mathbf{x}_a + \mathbf{F}_4(V_{eq})\hat{\mathbf{D}}_a\mathbf{u}, \end{aligned} \tag{19}$$

where the modified state-space matrices are now independent of the equivalent airspeed, and the influence of the airspeed is collected in the matrices $\mathbf{F}_1$ to $\mathbf{F}_4$. These matrices are found by taking out the dependencies of the equivalent airspeed during the formulation of the state-space system. As a result, the characteristics of the state matrix will remain the same for different velocities, validating the assumption that dominant aerodynamic modes for different velocities can be assumed to be the same.

Before describing the effect of Mach number on the mode shapes, the effect of the change in aspect ratio on the mode shapes is investigated. In Figure 11 the mode shapes for a backward swept wing are shown for 4 different aspect ratios of the wing. The aspect ratios are 9.5, 8, 6.5 and 5. Please note that only the shapes along the chordwise and spanwise directions with the origin at the root trailing edge point are displayed to enable a good comparison between the mode shapes for different aspect ratios.

The mode shapes for the first three, most dominant modes, are practically constant with changing the aspect ratio of the wing. Up to mode 7 the shapes remain very similar. As the mode number increases further, a larger difference is seen with increasing aspect ratio, although the trend is still similar. A similar trend is also observed for a forward swept wing. A conclusion can then be made that the shapes for the first

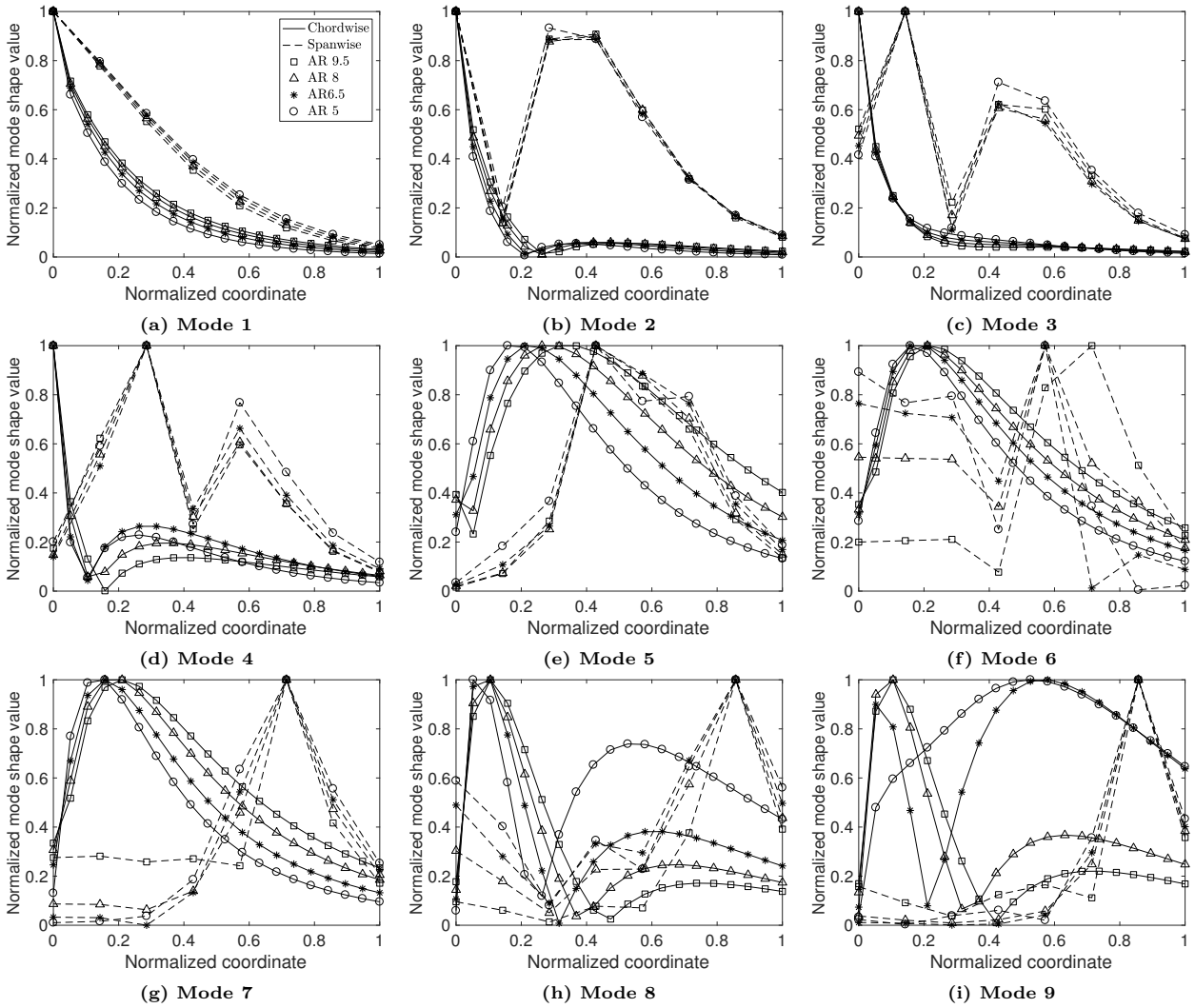


**Figure 11: First 9 BPOD mode shapes for a untapered, swept backward wing for different aspect ratios.**

7 dominant aerodynamic modes remain almost similar for different aspect ratio.

With respect to the Mach number effects, the application of Prandtl Glauert transformation brings the parametric dependency of the aerodynamic system on the Mach number. The Prandtl Glauert transformation scales the geometry in the x-direction by a factor $\sqrt{1-M^2}$, effectively changing the aspect ratio of the wing. The first seven dominant modes of the aerodynamic system stay nearly constant with the change in the aspect ratio. Hence, a change in Mach number results in a nearly no change in the dominant modes. Thus, with the assumptions mentioned before, a reduced basis constructed at one flight point can reasonably span the entire flight envelope.

### *2.4. Aeroelastic Framework*

In the present work, the reduced-order aerodynamic system, as described in the previous section, generated using BPOD, replaces the full order unsteady aerodynamic model in the PROTEUS framework. For the purpose of completeness, the state-space equation for the coupled dynamic system is derived. The governing equation of a linear dynamic structural model is given by:

$$\mathbf{M}\ddot{\mathbf{p}} + \mathbf{K}\mathbf{p} = \mathbf{F}_s \tag{20}$$

where $\mathbf{M}$ is the global mass matrix, $\mathbf{K}$ is the global stiffness matrix, $\mathbf{p}$ contains the structural degrees of freedom and $\mathbf{F}_s$ is the force vector. This system of equations can be converted to a first order state-space system by including both $\dot{\mathbf{p}}$ and $\mathbf{p}$ in the vector of state variables, resulting in:

$$\begin{pmatrix} \ddot{\mathbf{p}} \\ \dot{\mathbf{p}} \end{pmatrix} = \begin{bmatrix} \mathbf{0} & -\mathbf{M}^{-1}\mathbf{K} \\ \mathbf{I} & \mathbf{0} \end{bmatrix} \begin{pmatrix} \dot{\mathbf{p}} \\ \mathbf{p} \end{pmatrix} + \begin{bmatrix} \mathbf{M}^{-1} \\ \mathbf{0} \end{bmatrix} \begin{pmatrix} \mathbf{F}_s \\ \mathbf{0} \end{pmatrix} \tag{21}$$

$$\begin{pmatrix} \ddot{\mathbf{p}} \\ \dot{\mathbf{p}} \end{pmatrix} = \mathbf{A}_s \begin{pmatrix} \dot{\mathbf{p}} \\ \mathbf{p} \end{pmatrix} + \mathbf{B}_s \begin{pmatrix} \mathbf{F}_s \\ \mathbf{0} \end{pmatrix} \tag{22}$$

where $\mathbf{I}$ is the identity matrix, $\mathbf{0}$ the zero matrix, and $\mathbf{A}_s$ and $\mathbf{B}_s$ the structural state and input matrices, respectively. Coupling Equations 7 and 22 and performing some algebraic manipulation, results in the reduced-order dynamic aeroelastic state-space system:

$$\begin{aligned} \dot{\mathbf{x}} &= \mathbf{A}_{ae}\mathbf{x} + \mathbf{B}_{ae}\mathbf{u} \\ \begin{pmatrix} \mathbf{F} \\ \mathbf{p} \end{pmatrix} &= \mathbf{C}_{ae}\mathbf{x} + \mathbf{D}_{ae}\mathbf{u} \end{aligned} \tag{23}$$

where the state vector $\mathbf{x}$ is given by $\begin{bmatrix} \mathbf{c} & \dot{\mathbf{p}} & \mathbf{p} \end{bmatrix}^T$, $\mathbf{F}$ contains unsteady lift and moment forces and $\mathbf{A}_{ae}$, $\mathbf{B}_{ae}$, $\mathbf{C}_{ae}$ and $\mathbf{D}_{ae}$ are the aeroelastic state, input, output and feedthrough matrices.

### *2.5. Common Research Model*

The NASA CRM [26], originally developed for the 4th AIAA drag prediction workshop, is used as a case study for the current analysis. The main characteristics of the aircraft are summarized in Table 3. Figure 12 depicts the wing planform. The wing consist of 54 ribs with a rib spacing of 0.55 m that are taken into account as concentrated masses. Additionally, fuel, engine, leading edge devices and trailing edge devices are also accounted for as concentrated masses. The top and bottom skin of the wing is strengthened with the help of stringers that run along the span of the wing.

**Table 3: Characteristics of the CRM wing.**

| **Parameter** | **Value** |
|---|---|
| Span | 58.769 m |
| Leading edge sweep angle | 35 deg |
| Wing aspect ratio | 8.4 |
| Taper ratio | 0.275 |
| Planform wing area | 412 $m^2$ |
| Cruise Mach | 0.85 |
| Design Range | 14,300 km |
| Design Payload | 45,000 kg |
| Maximum takeoff weight | 296,000 kg |

### *2.6. Response to Varying Gust Length*

To demonstrate the application of the reduced-order aeroelastic framework in determining the gust response of aircraft, the CRM wing model is subjected to a discrete 1-cosine gust of varying gust lengths. The 1-cosine profile for the discrete gust is given by [4]

$$U = \frac{U_{ds}}{2}\left(1 - \cos\left(\frac{\pi s}{H}\right)\right) \tag{24}$$

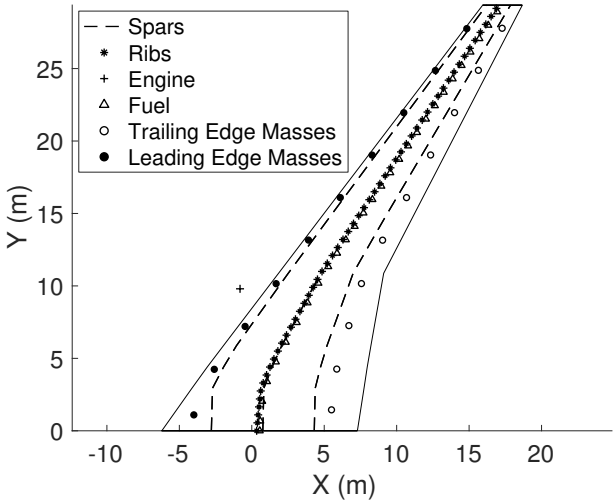


**Figure 12: CRM wing planform.**

where $U$ is the gust velocity, $s$ the distance penetrated into the gust, $H$ the gust gradient, and $U_{ds}$ the design gust velocity defined as

$$U_{ds} = U_{ref} F_g \left( \frac{H}{350} \right)^{1/6} \tag{25}$$

where $U_{ref}$ is the reference velocity that reduces bi-linearly from 17.07 m/s at sea level to 13.41 m/s at 4,572 m and then to 6.36 m/s at 18,288 m, and $F_g$ is the flight profile alleviation factor related to the aircraft maximum take-off weight and maximum landing weight.

Figure 13 depicts the four different gust velocity profiles having gust gradients of 9 m, 30 m, 80 m and 110 m. Figures 14 and 15 depict the root bending moment and root torsional moment responses of the CRM wing to the four different gust gradients as obtained by the FOM and the ROAM, using 20 out of 1188 modes, for a flight point of $M = 0.73$ at an altitude of 11,000 m. As can be seen, the error in the responses from the ROAM as compared to the responses from the FOM is less than 0.5% across the entire time history. With respect to computational efficiency, the ROAM took 160 s to build and 1.2 s to simulate whereas the FOM took 29.3 s to simulate. The time required for building the ROAM outweighs the benefit in this case, because only a small number of flight points are included. The simulation time, however, is decreased by 96%, so if more flight points will be included, the reduction in simulation time will at some point outweigh the time spend on building the ROAM, as is demonstrated in the next subsection.

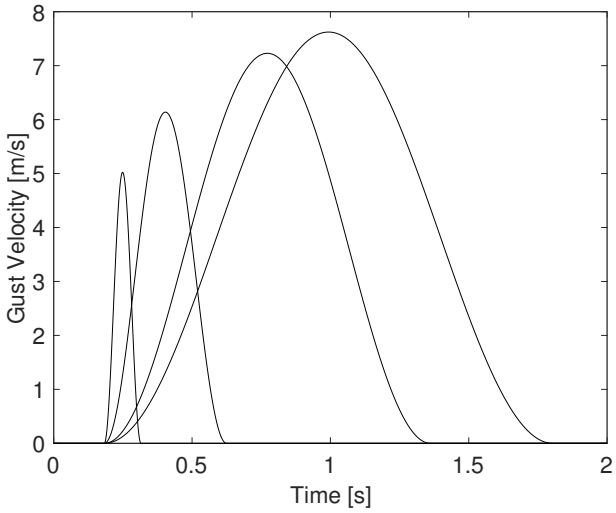


**Figure 13: Gust Profile for different gust gradients.**

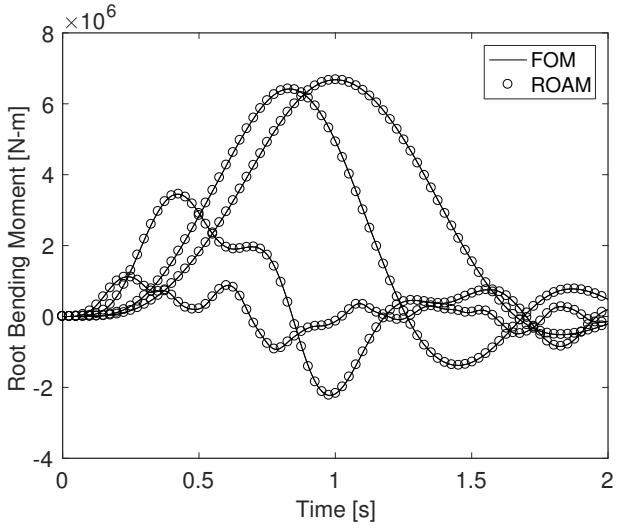


**Figure 14: Root bending moment response for the FOM and ROAM of the CRM wing.**

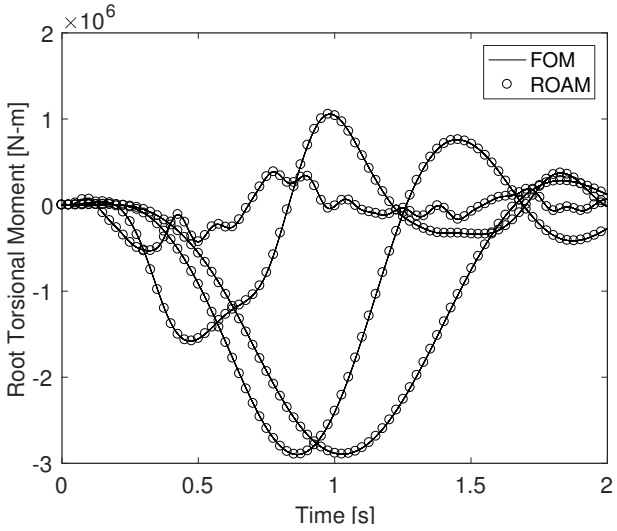


**Figure 15: Root torsional moment response for the FOM and ROAM of the CRM wing.**

### *2.7. Response across the flight envelope*

To demonstrate the applicability of the reduction method, the response of the standard backward swept CRM wing and a forward swept version of the CRM wing using both the ROAM and the FOM is evaluated at 36 different flight points across the flight envelope. For each flight point, 68 different gust gradients, ranging from 9 m to 107 m, are considered, bringing the total number of evaluated flight points to 2448. For the froward swept version, a forward sweep of 36 degrees is applied on the leading edge. Table 4 gives a summary of the different flight conditions considered in this study. A reduced basis is calculated at the cruise condition with a cruise speed of 220 m/s at 10 km altitude and a Mach number of 0.73. The altitude has been reduced from the standard 11 km to 10 km in order to bring down the Mach number and remain within the validity of the high subsonic potential flow theory. The first 20 out of a total of 1188 aerodynamic modes of this basis are used as the global reduced basis for the ROAM.

**Table 4: List of flight points.**

| Flight parameter | Number |
|---|---|
| Flight speed | 3 |
| Altitude | 12 |
| Gust gradient | 68 |
| Total number of points | 2,448 |

The load plots over the complete flight envelope, also called potato plots, for combination of root bending moment, root shear force and root torsional moment for both backward swept wing and forward swept wing are shown in Figures 16, 17, 18 and 19. A good agreement of the ROAM with the FOM across the entire flight envelope is obtained with the maximum error being less than 0.5%.

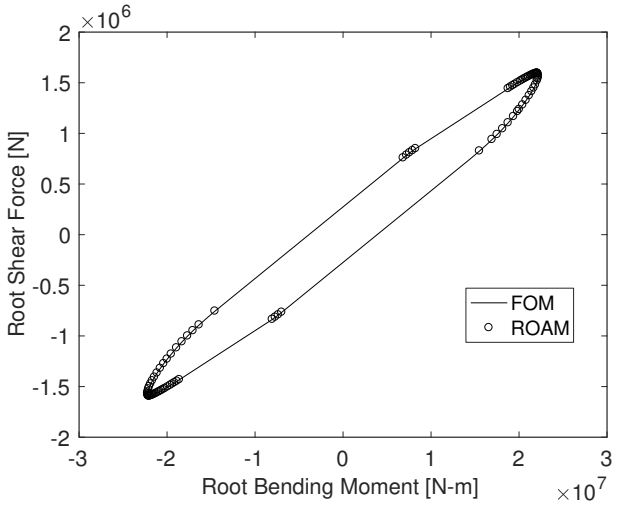


**Figure 16: Root bending moment versus shear force for the backward swept CRM.**

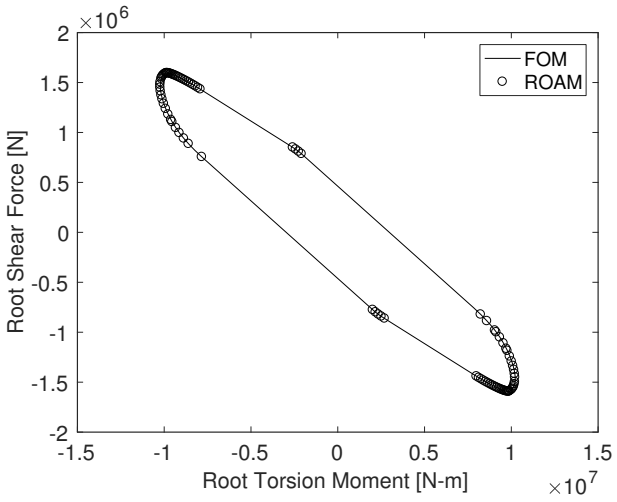


**Figure 17: Root torsion moment versus shear force for the backward swept CRM.**

Table 5 compares the computational effort required by the FOM and the ROAM for sweeping the flight envelope. The time related to the model setup for the ROAM is kept low by using the single reduced basis as the global basis, as was explained before. The achieved reduction in simulation time is an order of magnitude larger than the extra time required for creating the ROAM, resulting in an 85.5% saving in the computational effort in identifying the critical loads.

**Table 5: Breakdown of computational time required for the critical load identification (Values in the bracket indicate savings in computational time of ROAM simulations with respect to FOM simulations in terms of percentage).**

| | **Model setup** (min) | **Simulation time** (min) | **Total time** (min) |
|---|---|---|---|
| FOM | 0 | 171 | 171 |
| ROAM | 2.7 | 22.1 | 24.8 |
| Difference | 2.7 (-) | 148.9 (87.1%) | 146.2 (85.5%) |

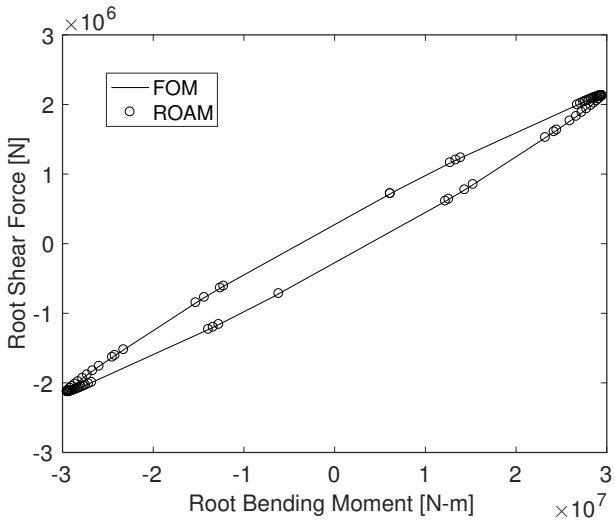


**Figure 18: Root bending moment versus shear force for the forward swept CRM.**

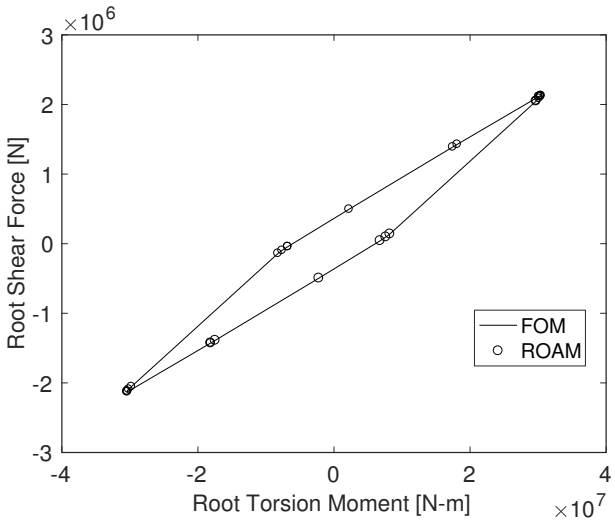


**Figure 19: Root torsion moment versus shear force for the forward swept CRM.**

## 3. Optimization Framework

As has been mentioned before, in the case of gust loads, there is no prior information on the flight point which leads to the critical load. During the optimization process, for every iteration, an update in the design of the wing would lead to a modification in the aeroelastic characteristics of the wing, which could result in a different critical gust load. As a result, at every iteration, a range of load cases across the entire flight envelope needs to be evaluated to determine the worst case gust load. Hence an optimization framework, depicted in Figure 20, is formulated which has the capability to determine the critical gust load at every iteration in a computationally efficient manner. It starts with the identification of the worst gust load for the initial design using the ROAM. Next, for the given critical dynamic and static load conditions, PROTEUS analyses the initial design and calculates the analytical sensitivities which are then fed to the optimizer. Optimizer calculates the new design variables which are fed to ROAM as well as PROTEUS. ROAM analyzes the entire flight envelope with respect to the new design variables, identifies the critical loads and feeds it back to PROTEUS. The process continues until an optimum has been reached. Since the analytical sensitivities of the objective function and constraints, including the sensitivities of the critical dynamic loads, are available, the gradient based optimizer Globally Convergent Method of Moving Asymptotes (GCMMA) developed by Svanberg [39] is used.

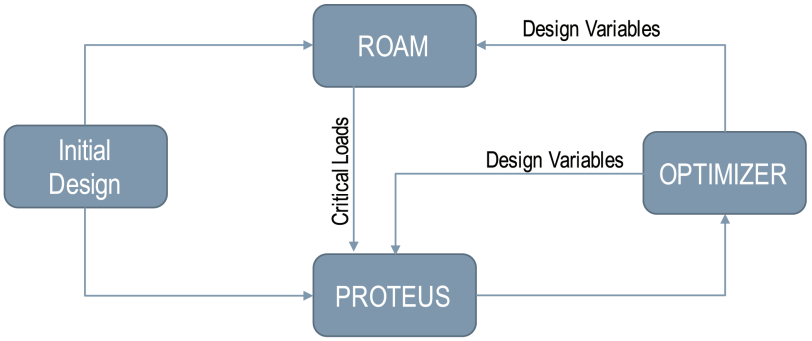


**Figure 20: Schematic representation of the optimization framework.**

*3.1. Optimization Setup*

References [40–43] have performed aero-structural sizing and optimization of the aforementioned CRM wing subjected to only static loads. Stodieck et al. [44] performed aeroelastic tailoring of the CRM wing by also taking into account the gust loads. Stodieck et al. used only 3 flight points to analyse the gust loads and these flight points were also kept constant during the optimization. In the current study, for the aeroelastic tailoring of the CRM wing, clamped at root, gust load analysis is carried out on 64 flight points and at every iteration, to identify the critical gust loads, all the 64 points are evaluated. Table 6 shows the material properties used for the CRM wing. To account for the effect of material scatter, barely visible impact damage and environmental effects, the strength allowables are knocked down by a factor of 0.416 [45]. Table 7 gives the information regarding the optimization setup considered in the current study. The objective is to minimize the structural weight of the wing. The wing is divided into 10 spanwise sections. Each section of the top skin and the bottom skin consists of two laminates in the chordwise direction and each section of each spar has one laminate. This distribution results in 64 unique laminates. The laminates are represented by lamination parameters which describe the in-plane and out-of-plane behaviour of the composite laminates which are symmetric and unbalanced. For every laminate, there are eight lamination parameters and one thickness variable resulting in a total number of 576 design variables. Figure 21 depicts the laminate distribution along the top skin of the wing. It also shows the stiffness for each laminate, where the wing stiffness distribution is represented by the polar plot of thickness normalized modulus of elasticity $\hat{\mathbf{E}}_{11}(\theta)$ which is given by

$$\hat{\mathbf{E}}_{11}(\theta) = \frac{1}{\hat{\mathbf{A}}_{11}^{-1}(\theta)} \tag{26}$$

where $\hat{\mathbf{A}}$ is the thickness normalized membrane stiffness matrix and $\theta$ ranges from 0 to 360 degrees.

**Table 6: Material Properties.**

| Property | Value |
|---|---|
| $E_{11}$ | 147 GPa |
| $E_{22}$ | 10.3 GPa |
| $G_{12}$ | 7 GPa |
| $\nu_{12}$ | 0.27 GPa |
| $\rho$ | 1600 kg/m$^3$ |
| $X_t$ | 2280 MPa |
| $X_c$ | 1725 MPa |
| $Y_t$ | 57 MPa |
| $Y_c$ | 228 MPa |
| $S$ | 76 MPa |

**Table 7: Optimization Setup.**

| Type | Parameter | # responses |
|---|---|---|
| Objective | Minimize Wing Mass | 1 |
| Design Variables | Lamination Parameter | 576 |
| | Laminate Thickness | |
| Constraints | Laminate Feasibility | 384 |
| | Static Strength | 1024/load case |
| | Buckling | 4096/load case |
| | Aeroelastic Stability | 10/load case |
| | Aileron Effectiveness | 1/load case |
| | Local Angle of Attack | 22/load case |

Lamination feasibility equations formulated by Hammer et al. [46], Raju et al. [47] and Wu et al. [48] are applied to make sure that the lamination parameters represent actual ply distributions. The static strength of the laminate is assessed by the failure envelope calculated using Tsai-Wu criterion formulated for lamination parameter domain by Khani et al. [49]. The stability of the panel in buckling is based on an idealized buckling model formulated by Dillinger et al. [50]. To ensure that the wing is aeroelastically stable, the real part of the eigenvalues of the state matrix should be less than zero within the flutter flight envelope. The local angle of attack is constrained to a maximum of 12 degrees and a minimum of -12 degrees. The aileron effectiveness computed as the negative ratio of the roll coefficient induced by the aileron deflection and the roll coefficient due to the roll manoeuvre, is set to a minimum of 0.1 to ensure reasonable handling quality [50].

Table 8 gives the information on the static load cases which are used for the current study. These load cases provided by NASA, represent the cruise condition, 2.5g symmetric pull up manoeuvre and -1g symmetric push down manoeuvre. With respect to dynamic load cases, 84 flight points covering the entire flight envelope are investigated. For each flight point, 40 gust gradient both positive as well as negative,

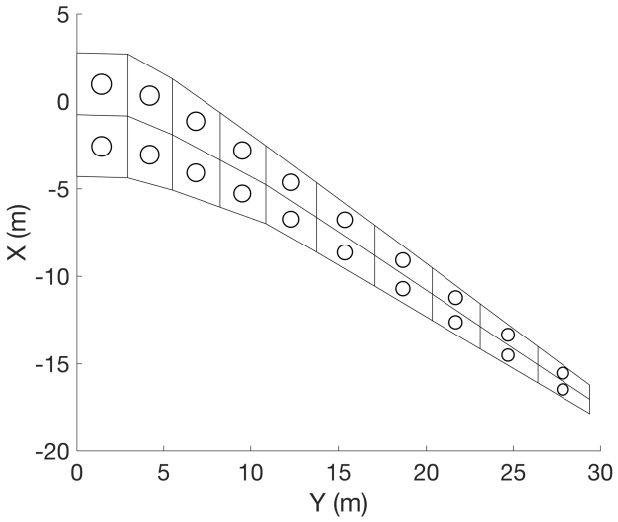


**Figure 21: Laminate Distribution of the top skin of CRM.**

ranging from 9 m to 107 m are considered. To simulate the effect of different mass configurations on the dynamic loads, 40 different fuel configurations were selected for initial evaluation. These configurations were selected based on requirements given by EASA CS-25 [4] which states that:

1. Load combinations must include each fuel load in the range from zero fuel to the selected maximum fuel.
2. Any critical fuel loading conditions, not shown to be extremely improbable, which may result from mismanagement of fuel.

Out of these 40 configurations, 6 critical combinations, depicted in Table 9, are included in the dynamic loads analysis. Thus, in total, 20,160 load cases will be scanned to determine the critical loads. Figure 22 displays the flight envelope with their respective flight point ID. For each gust load case, the wing response is analyzed at six time instances namely maximum and minimum root bending moment, maximum and minimum tip displacement and maximum and minimum tip twist. It will be shown later in the results part of the paper that with these six instances, the most critical load on the wing across the entire time history of the gust can be approximated.

**Table 8: List of Static Loadcases.**

| **Loadcase ID** | **$V_{eq}$** (m/s) | **Altitude** (m) | **Load Factor** | **Fuel level/Max fuel** (%) |
|---|---|---|---|---|
| 1 | 136 | 11000 | 1 | 70 |
| 2 | 240 | 3000 | 2.5 | 80 |
| 3 | 198 | 0 | -1 | 80 |

**Table 9: Details of Fuel Configurations Considered in Dynamic Load Cases.**

| Fuel Mass Case ID | Fuel Tank 1 (%) | Fuel Tank 2 (%) | Fuel Tank 3 (%) | Fuel Tank 4 (%) |
|---|---|---|---|---|
| 1 | 0 | 0 | 0 | 0 |
| 2 | 80 | 0 | 0 | 0 |
| 3 | 0 | 0 | 0 | 80 |
| 4 | 0 | 0 | 80 | 80 |
| 5 | 80 | 0 | 0 | 80 |
| 6 | 80 | 80 | 80 | 80 |

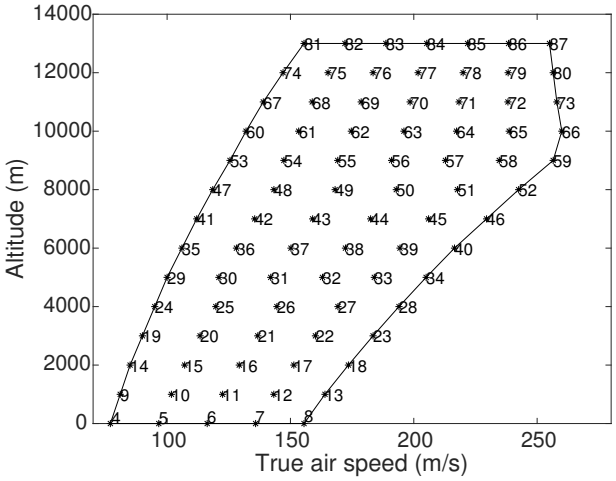


**Figure 22: Flight Envelope.**

*3.2. Results*

It took 42 iterations to obtain an optimized configuration resulting in a structural weight of 8,684 $kg$ which is 86.5% of the initial weight. Figure 23 shows the stiffness and the thickness distribution of the optimized CRM wing. The strain, and buckling constraints can be seen in Figure 24. The inner half of the wing is mainly dominated by strain and buckling constraints, whereas the outer half is dominated by aileron efficiency and strain constraints. In the inner half, the region near the wing root is dominated by buckling and as a result, the out of plane stiffness properties are more pronounced as compared to the rest of the wing. The middle part of the wing is sized by the strain and hence the in-plane stiffness are oriented along the wing axis to maximize the load carrying capabilities of the wing. The thickness in the inner half of the wing increases from the root till the region around the engine. Additionally, the front part has a higher thickness as compared to the aft, thus shifting the elastic axis forward and introducing wash-out twist upon wing bending which alleviates the load. In the outer half of the wing, the in-plane stiffness are oriented aft to increase the aileron effectiveness. Furthermore, the aft part is thicker than the front part, shifting the elastic axis aft thus making it beneficial in terms of aileron effectiveness.

Figures 25 and 26 depict the critical loads at various iterations in the optimization process on the top and bottom skin of the CRM wing respectively. For each laminate, the number outside the bracket indicates the critical flight point, the number inside the bracket indicates the fuel mass case ID and the colour indicates the critical gust gradient. The laminates with grey colour are critical with respect to the static load cases. Flight points 1, 2 and 3 are static load cases described in Table 8 and the rest are the dynamic flight points as shown in the Figure 22.

Looking at the critical loads, the change in the design variables leads to modification in the aeroelastic properties of the wing, which results in the variation of critical loads. Figure 27 shows the mean change in

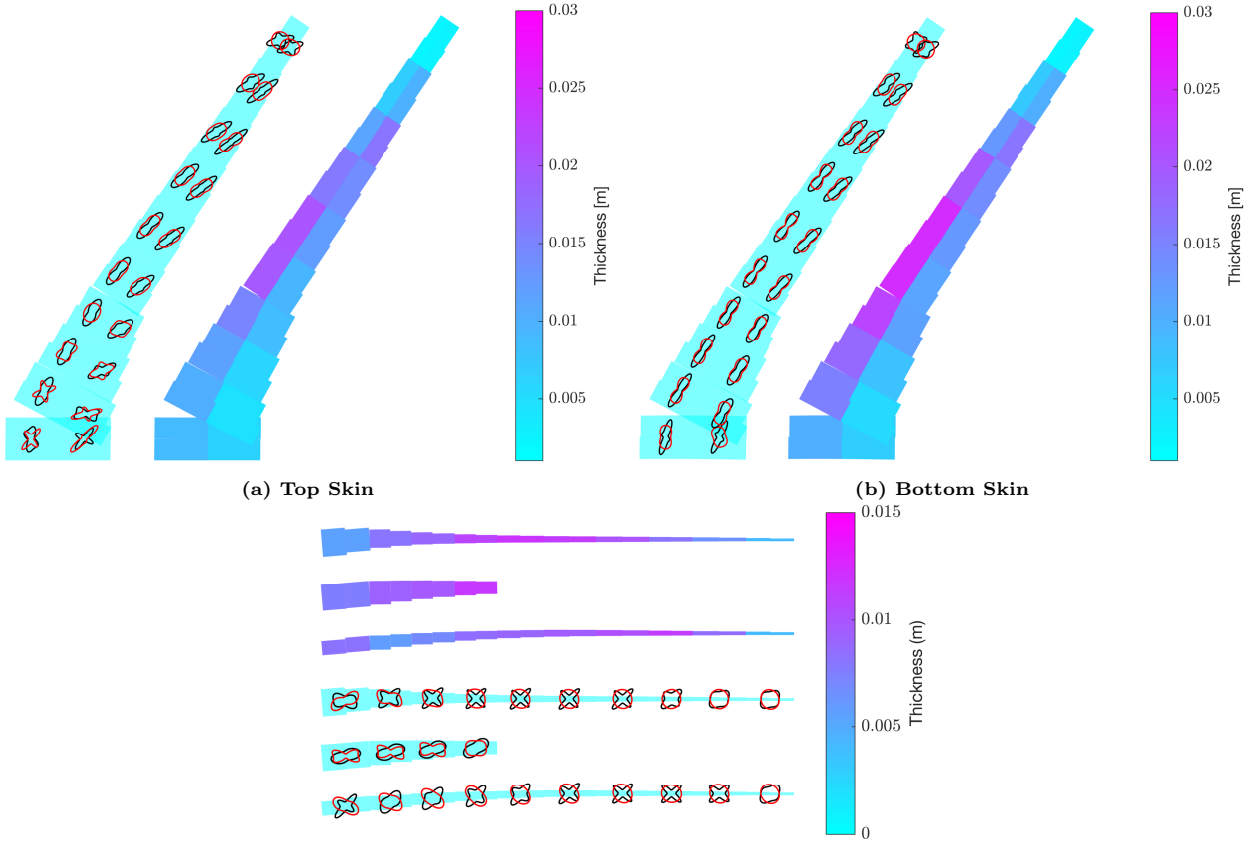


**(a) Top Skin** **(b) Bottom Skin**

**(c) Spars**

**Figure 23: Stiffness and thickness distribution for the optimized CRM wing (In-plane stiffness: black, out-of-plane stiffness: red).**

the design variables along the optimization process and Figure 28 shows the corresponding change in the frequency of the first bending mode. Additionally, Figure 29 shows for every iteration, the number of critical load cases that have been added or removed with respect to the previous iteration. As can be seen, the biggest change in the design variable as well as the first bending mode frequency happens in the first few iterations. As a result, the change in the critical loads is also significant in the first few iterations. Thus, in the case of the dynamic aeroelastic optimization process, the worst case gust loads need to be determined at every new iteration during the first few steps as the change in the later steps is minimal.

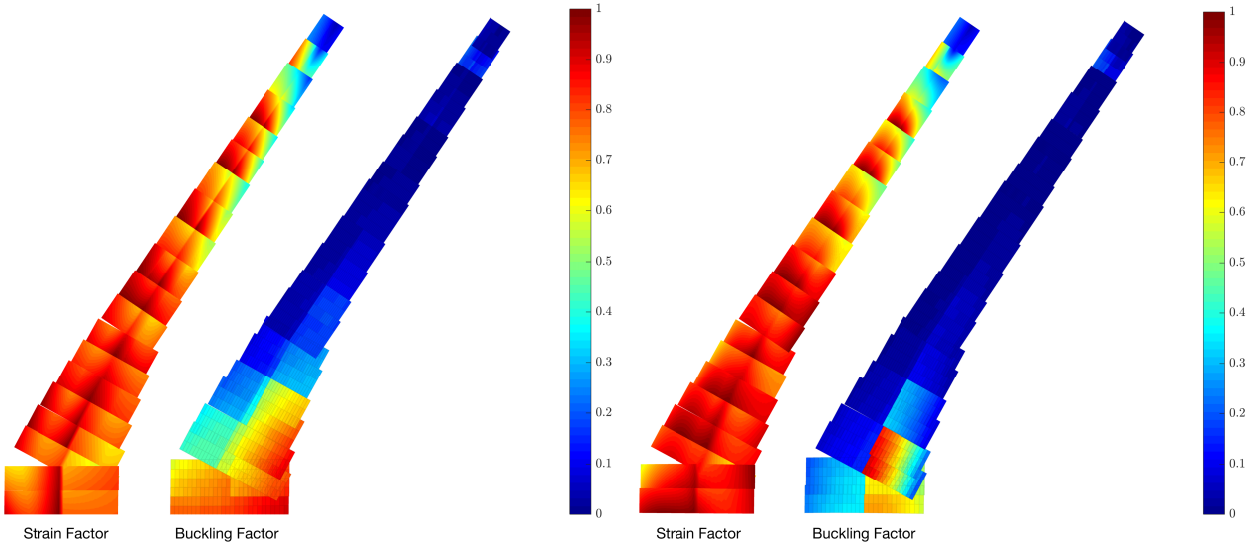


**(a) Top Skin**




**(b) Bottom Skin**

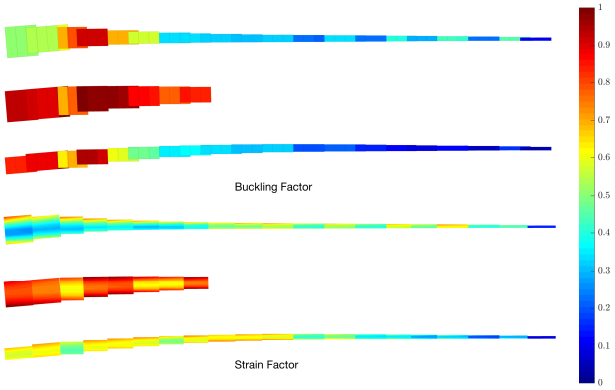


**(c) Spars**

**Figure 24: Strain and buckling factor distribution on the optimized CRM wing.**

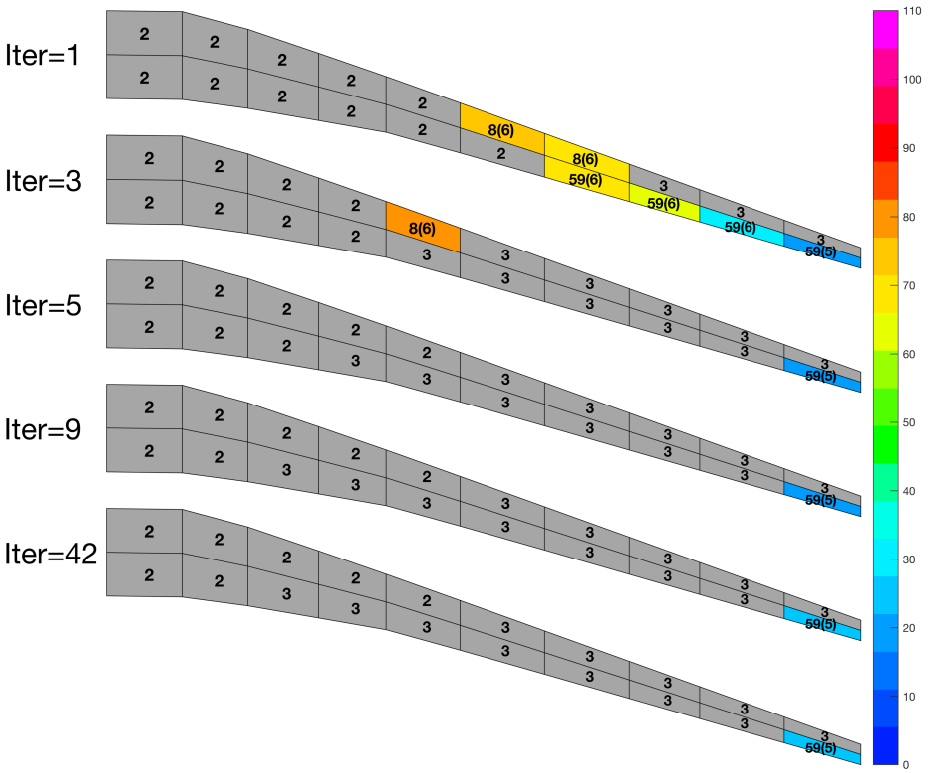


**Figure 25: Critical flight points and gust gradients on the top skin during the optimization process.**

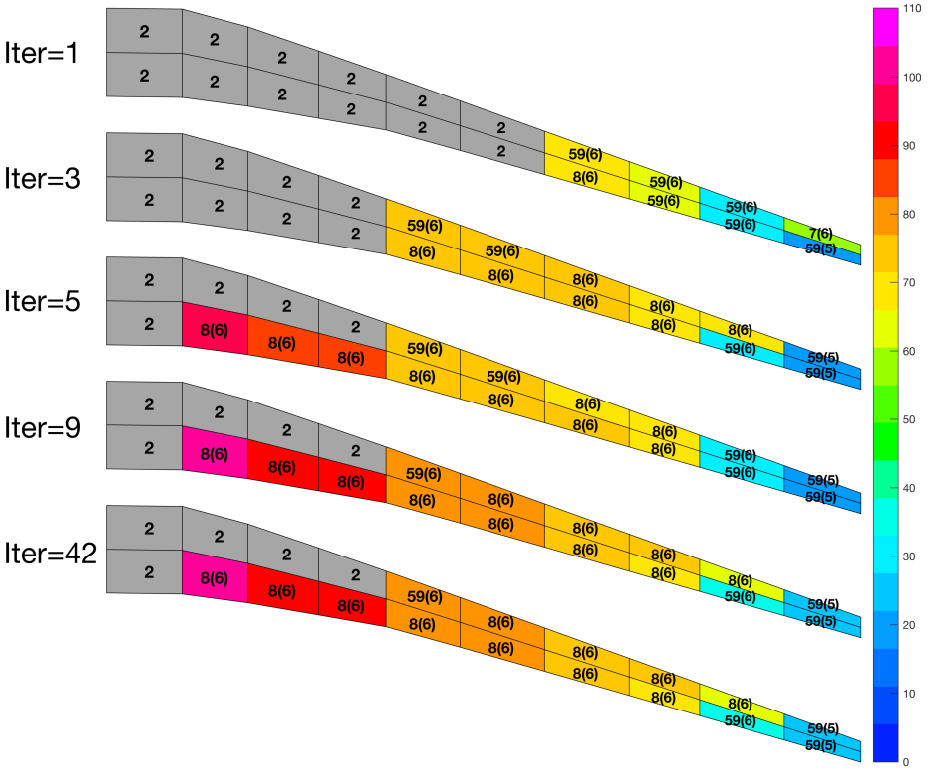


**Figure 26: Critical flight points and gust gradients on the bottom skin during the optimization process.**

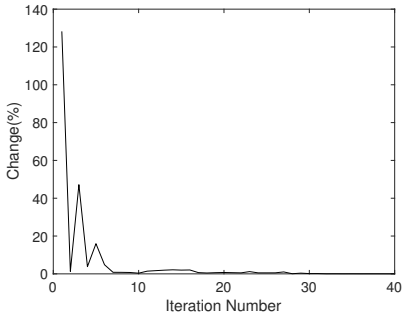


**Figure 27: Mean change in the design variables.**

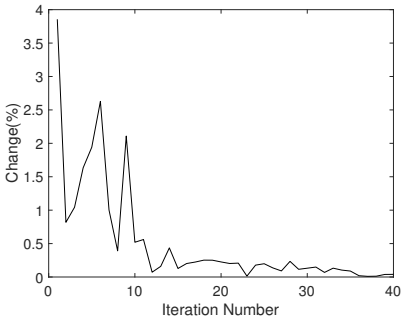


**Figure 28: Change in the 1st bending frequency.**

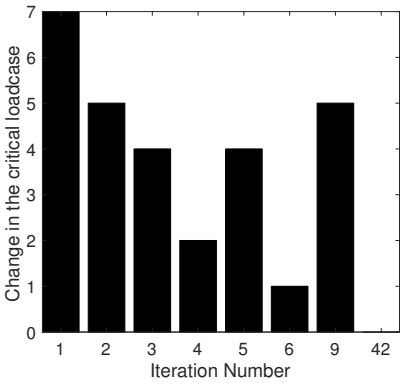


**Figure 29: Total number of the change in the critical load cases.**

To understand the importance of updating critical loads during the optimization process, the CRM wing is optimized with respect to the critical loads determined only for the initial design. Figure 30 shows the maximum strain factor for each laminate of the optimized wing obtained by analyzing the entire flight envelope. As can be seen, the optimized wing violates the strain constraints by a maximum of 5 %. This is due to the fact that the critical loads are different than the loads that the wing is optimized for. Although for the current design, the maximum violation is of only 5%, in the area of loads, such a small violation can cause a huge penalty in terms of weight of the wing. Additionally, the magnitude of the violation depends on how close the initial design is with respect to the optimum configuration. If there is a big difference, then the violation could be bigger as well. The failure of the optimized wing under gust loads illustrates the importance of identifying gust loads at various iteration in the design process.

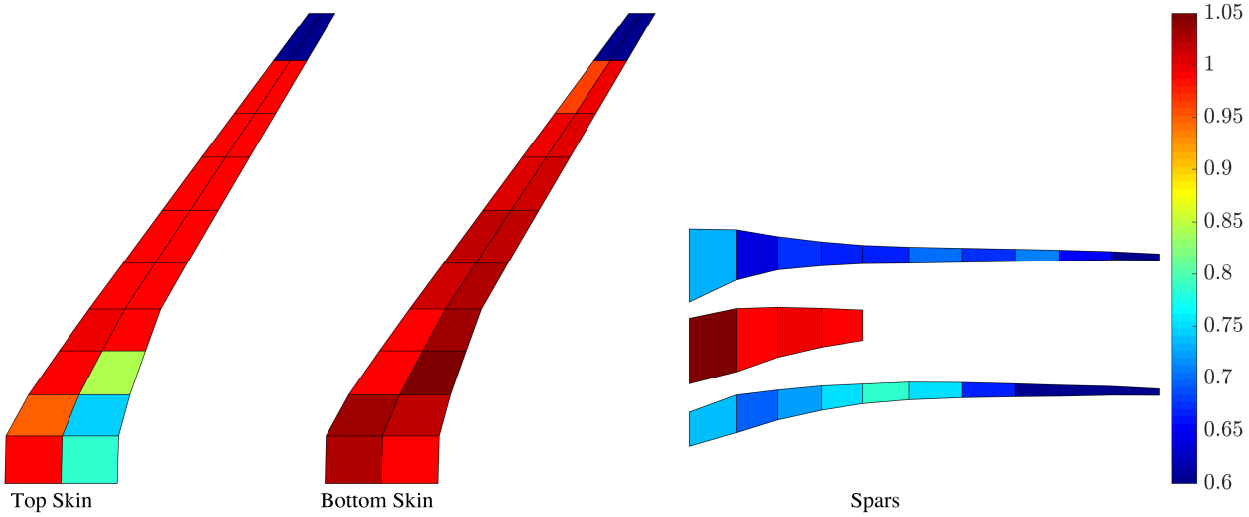


**Figure 30: Strain factor distribution of the CRM wing optimized with a fixed set of critical loads.**

Gust response is dominated by the dynamic pressure and the reference gust velocity. As per the certification requirements, the reference gust velocity decreases as the altitude increases. Hence, along with cruise load case, the points at sea level also are responsible for the critical gust loads. With respect to gust gradient, critical length increases as we move from the outer part towards the inner part of the wing. And with respect to fuel mass configurations, fuel mass case 6 is the critical fuel mass case for the entire wing except for the outer laminates in which fuel mass case 5 becomes critical.

It should be noted that the present study is performed on a clamped wing only. Due to the flight

dynamics, the gust loads on a free flying aircraft are usually lower than on a clamped wing, however, the critical gust load cases are still expected to change during the optimization process. The methodology, proposed to identify critical gust loads at every iteration and include it in the optimization for the clamped wings, can be adapted to a free flying aircraft as well.

As was mentioned before, the wing response is evaluated at six instances per gust load. To prove the validity of this approach, the highest strain factor for the optimized wing is calculated by analyzing wing response at every instance of the time history and compared with the highest strain factors analyzed by taking into account only 6 aforementioned instances in the response. Figure 31 shows the increase in strain factor by taking the entire time history into account. The highest difference is about 0.5%, thus validating the approach taken.

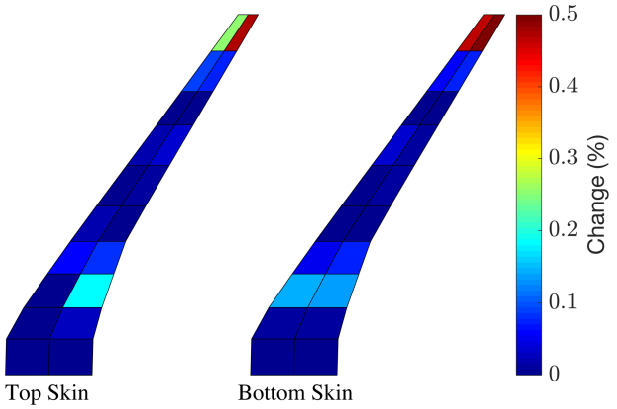


**Figure 31: Comparison of the strain factor determined for the entire time history with strain factor determined only at 6 aforementioned instances.**

## 4. Conclusions

In this paper, a dynamic aeroelastic optimization method was formulated using the ROAM. The ROAM which is based on PROTEUS was created by reducing the order of the unsteady vortex lattice model and coupling it to the structural solver. To find a suitable MOR method for such an aerodynamic model, MT, BT, POD, and BPOD methods when applied to the unsteady vortex lattice model were investigated by applying them to two test cases. The combination of high accuracy with very few states, relatively low computational cost for a typical model size of interest, and sufficient robustness, made the BPOD the most suitable MOR method for the aeroelastic framework.

The ROAM formulated using the BPOD method predicts the wing responses caused by different gust gradients very accurately. To be able to efficiently cover the complete flight envelope of an aircraft for a given wing planform, a new formulation for the state-space system was derived where the influence of the equivalent airspeed was isolated from the state-space matrices. Furthermore, it was demonstrated that the Mach number, which in this vortex lattice model is implemented using the Prandtl-Glauert correction, has a negligible effect on the reduced basis. A single ROM could thus be used to analyze the aeroelastic loads throughout the flight envelope, reducing the computational cost significantly. The comparison of the loads acting on a backward and forward swept version of the NASA CRM obtained with the ROAM and FOM proved the validity of the assumption. A considerable saving in computational cost of about 89% for the analysis of 2448 flight points, was obtained using this method.

Using the developed ROAM, a dynamic aeroelastic optimization framework was formulated and thickness and stiffness optimization of the CRM wing clamped at the root was carried out. The results showed that both static as well as gust loads are critical for a composite clamped wing. Furthermore, the change in the design variables was highest during the first few iterations which lead to a considerable change in the

critical loads in the first few iterations. This showed the importance of updating the critical loads along the dynamic aeroelastic optimization process.

## References


[1] A. Krein, G. Williams, Flightpath 2050: Europe's vision for aeronautics, Innovation for Sustainable Aviation in a Global Environment: Proceedings of the Sixth European Aeronautics Days, Madrid, 30 March-1 April, 2011 (2012) 63.

[2] N. P. M. Werter, Aeroelastic modelling and design of aeroelastically tailored and morphing wings, Ph.D. thesis, Delft University of Technology (2017).

[3] D. N. Mavris, D. A. DeLaurentis, Methodology for examining the simultaneous impact of requirements, vehicle characteristics, and technologies on military aircraft design, in: $22^{nd}$ Congress of ICAS, 2000.

[4] European Aviation Safety Agency, Certification Specifications and Acceptable Means of Compliance for Large Aeroplanes CS-25, 15 July 2015, amendment 17.

[5] H. H. Khodaparast, G. Georgiou, J. E. Cooper, L. Riccobene, S. Ricci, G. Vio, P. Denner, Efficient worst case 1-cosine gust loads prediction, Journal of Aeroelasticity and Structural Dynamics 2 (3).

[6] A. S. Pototzky, T. A. Zeiler, B. PERRY III, Calculating time-correlated gust loads using matched filter and random process theories, Journal of Aircraft 28 (5).

[7] K. J. Fidkowski, F. Engelsen, K. E. Willcox, I. M. Kroo, Stochastic gust analysis techniques for aircraft conceptual design, in: 12th AIAA/ISSMO Multidisciplinary Analysis and Optimization Conference, 2008, p. 5848.

[8] A. Knoblach, Robust performance analysis applied to gust loads computation, Journal of Aeroelasticity and Structural Dynamics 3 (1).

[9] H. H. Khodaparast, J. E. Cooper, Worst case gust loads prediction using surrogate models and system identification methods, in: Proceedings of 54th AIAA/ASME/ASCE/AHS/ASC Structures, Structural Dynamics and Materials Conference, Boston, MA, 2013.

[10] L. Cavagna, S. Ricci, L. Riccobene, Fast-glp: a fast tool for the prediction of worst case gust loads based on neural networks, in: 54th AIAA/ASME/ASCE/AHS/ASC Structures, Structural Dynamics, and Materials Conference, 2013, p. 1493.

[11] C. Wales, A. Gaitonde, D. Jones, Reduced-order modeling of gust responses, Journal of Aircraft 54 (4) (2016) 1350–1363.

[12] S. P. Williams, D. Jones, A. Gaitonde, C. Wales, S. J. Huntley, Reduced order modelling of aircraft gust response for use in early design stages, in: 35th AIAA Applied Aerodynamics Conference, 2017, p. 3906.

[13] M. Bergmann, A. Ferrero, A. Iollo, H. Telib, An approach to predict gust effects by means of hybrid rom/cfd simulations, in: ECCOMAS 2016, 2016.

[14] R. Thormann, P. Bekemeyer, S. Timme, Reduced order modelling of gust analysis using computational fluid dynamics, in: ECCOMAS 2016, 2016.

[15] S. Timme, K. Badcock, A. Da Ronch, Gust analysis using computational fluid dynamics derived reduced order models, Journal of Fluids and Structures 71 (2017) 116–125.

[16] M. Reyes, H. Climent, M. Karpel, F. Arevalo, C. Maderuelo, Increased-order aeroservoelastic modeling in practice, in: Proceedings of the International Forum on Aeroelasticity and Structural Dynamics, 2017.

[17] T. Wilson, A. Azabal, A. Castrichini, J. Cooper, R. Ajaj, M. Herring, Aeroelastic behaviour of hinged wing tips, in: Proceedings of the International Forum on Aeroelasticity and Structural Dynamics, 2017.

[18] M. Castellani, Y. Lemmens, J. E. Cooper, Parametric reduced order model approach for rapid dynamic loads prediction, Aerospace Science and Technology 52 (2016) 29–40.

[19] N. P. M. Werter, R. De Breuker, M. M. Abdalla, Continuous-time state-space unsteady aerodynamic modeling for efficient loads analysis, AIAA Journal (2017) 1–12.

[20] E. J. Davison, A method for simplifying linear dynamic systems, IEEE Transactions on Automatic Control 11 (1) (1966) 93–101.

[21] K. C. Hall, Eigenanalysis of unsteady flows about airfoils, cascades and wings, AIAA Journal 32 (12).

[22] B. C. Moore, Principle component analysis in linear systems: Controllability, observability, and model reduction, IEEE Transactions on Automatic Control AC-26 (1981) 17–32.

[23] P. Holmes, J. L. Lumley, G. Berkooz, Turbulence, Coherent Structures, Dynamical Systems and Symmetry, 2nd Edition, Cambridge University Press, 2012.

[24] K. Willcox, J. Peraire, Balanced model reduction via the proper orthogonal decomposition, AIAA Journal 40 (11) (2002) 2323–2330.

[25] C. W. Rowley, Model reduction for fluids, using balanced proper orthogonal decomposition, International Journal of Bifurcation and Chaos in Applied Sciences and Engineering 15 (3) (2005) 997–1013.

[26] J. C. Vassberg, M. A. DeHaan, S. M. Rivers, R. A. Wahls, Development of a common research model for applied cfd validation studies, in: 26th AIAA Applied Aerodynamics Conference, Honolulu, Hawaii, 2008.

[27] N. P. M. Werter, R. De Breuker, A novel dynamic aeroelastic framework for aeroelastic tailoring and structural optimisation, Composite Structures 158 (2016) 369–386. doi:10.1016/j.compstruct.2016.09.044.

[28] J. Murua, R. Palacios, J. M. R. Graham, Applications of the unsteady vortex-lattice method in aircraft aeroelasticity and flight dynamics, Progress in Aerospace Sciences 55 (2012) 46–72.

[29] M. Behbahani-Nejad, H. Haddadpour, V. Esfahanian, Reduced-order modeling of unsteady flows without static correction requirement, Journal of Aircraft 42 (4).

[30] L. Pernebo, L. M. Silverman, Model reduction via balanced state space representations, IEEE transactions on automatic control 27 (2) (1982) 382–387.

[31] M. Ilak, C. W. Rowley, Modeling of transitional channel flow using balanced proper orthogonal decomposition, Physics of Fluids 20 (3) (2008) 034103. doi:10.1063/1.2840197.

[32] M. Behbahani-Nejad, M. Changizian, Eigenanalysis and reduced-order modelling of unsteady partial cavity flows using the boundary element method, Engineering Analysis with Boundary Elements 37 (2013) 1151–1160.
[33] K. C. Hall, J. P. Thomas, E. H. Dowell, Proper orthogonal decomposition technique for transonic unsteady aerodynamic flows, AIAA Journal 38 (10) (2000) 1853–1862. doi:10.2514/2.867.
[34] J. P. Thomas, E. H. Dowell, K. C. Hall, Three-dimensional transonic aeroelasticity using proper orthogonal decomposition-based reduced-order models, Journal of Aircraft 40 (3) (2003) 544–551. doi:10.2514/2.3128.
[35] P. Benner, S. Gugercin, K. Willcox, A survey of projection-based model reduction methods for parametric dynamical systems, SIAM Review 57 (4) (2015) 483–531. doi:10.1137/130932715.
[36] D. Amsallem, C. Farhat, An online method for interpolating linear parametric reduced-order models, SIAM Journal on Scientific Computing 33 (5) (2011) 2169–2198.
[37] T. Lieu, C. Farhat, M. Lesoinne, Reduced-order fluid/structure modeling of a complete aircraft configuration, Computer methods in applied mechanics and engineering 195 (41) (2006) 5730–5742.
[38] R. Schmit, M. Glauser, Improvements in low dimensional tools for flow-structure interaction problems: using global pod, in: APS Division of Fluid Dynamics Meeting Abstracts, Vol. 1, 2003.
[39] K. Svanberg, A class of globally convergent optimization methods based on conservative convex separable approximations, SIAM journal on optimization 12 (2) (2002) 555–573.
[40] C. V. Jutte, B. Stanford, C. D. Wieseman, J. B. Moore, Aeroelastic tailoring of the nasa common research model via novel material and structural configurations, in: 52nd Aerospace Sciences Meeting, 2014, p. 0598.
[41] T. Klimmek, Development of a structural model of the crm configuration for aeroelastic and loads analysis, in: Proceedings of the International Forum on Aeroelasticity and Structural Dynamics, 2013.
[42] S. Keye, T. Klimmek, M. Abu-Zurayk, M. Schulze, C. Ilic, Aero-structural optimization of the nasa common research model, in: 18th AIAA/ISSMO Multidisciplinary Analysis and Optimization Conference, 2017, p. 4145.
[43] G. K. Kenway, J. R. Martins, Multipoint high-fidelity aerostructural optimization of a transport aircraft configuration, Journal of Aircraft 51 (1) (2014) 144–160.
[44] O. Stodieck, J. Cooper, P. Weaver, P. Kealy, Aeroelastic tailoring of a representative wing box using tow-steered composites, AIAA journal (2016) 1425–1439.
[45] C. Kassapoglou, Design and analysis of composite structures: with applications to aerospace structures, John Wiley & Sons, 2013.
[46] V. B. Hammer, M. Bendsøe, R. Lipton, P. Pedersen, Parametrization in laminate design for optimal compliance, International Journal of Solids and Structures 34 (4) (1997) 415–434.
[47] G. Raju, Z. Wu, P. Weaver, On further developments of feasible region of lamination parameters for symmetric composite laminates, in: 55th AIAA/ASMe/ASCE/AHS/SC Structures, Structural Dynamics, and Materials Conference, 2014, p. 1374.
[48] Z. Wu, G. Raju, P. M. Weaver, Framework for the buckling optimization of variable-angle tow composite plates, AIAA Journal 53 (12) (2015) 3788–3804.
[49] A. Khani, S. T. IJsselmuiden, M. M. Abdalla, Z. Gürdal, Design of variable stiffness panels for maximum strength using lamination parameters, Composites Part B: Engineering 42 (3) (2011) 546–552.
[50] J. Dillinger, T. Klimmek, M. M. Abdalla, Z. Gürdal, Stiffness optimization of composite wings with aeroelastic constraints, Journal of Aircraft 50 (4) (2013) 1159–1168.